CONTRIBUTION OF ^{230}TH MEASUREMENTS TO THE ESTIMATION OF THE ABYSSAL CIRCULATION

Olivier Marchal[a], Roger François[b], and Jan Scholten[c]

[a] Woods Hole Oceanographic Institution
Woods Hole, MA 02543, USA
Tel: +1 508 289 3374
Fax: +1 508 457 2187
email: omarchal@whoi.edu

[b] Earth and Ocean Sciences
University of British Columbia
Vancouver, Canada

[c] IAEA Marine Environment Laboratory
Monaco, France

Deep-Sea Research (Part I), vol. 54 (4), 557–585, 2007

Abstract

An inverse finite-difference model of the abyssal circulation in the North Atlantic Ocean is developed in order to evaluate the dynamical information contained in measurements of thorium-230 (^{230}Th). The model has a very coarse resolution ($3° \times 3° \times 1000$ m) and is based on lowest order balances for planetary flows. The naturally occurring ^{230}Th differs from more conventional oceanic tracers in several respects, e.g., its production (by ^{234}U radioactive decay) is globally uniform to a good approximation and its removal can be understood in terms of a simple reversible exchange with particles sinking slowly to the seafloor. The time required for ^{230}Th to reach steady state with respect to particle exchange is estimated to increase with depth, reaching O(10) yr below 1000 m. In the North Atlantic ^{230}Th activities at distant locations share a similar increase with depth in the upper $\sim$ 1000 m – a pattern consistent with a reversible exchange – but show drastic differences in the abyssal interior. Two inversions are conducted in order to determine whether the ^{230}Th differences reflect the effects of the circulation – by preventing the slow attainment to steady state w.r.t. particle exchange in deep water – and provide complementary information about the abyssal flow. In a first inversion, observations of density from a hydrographic compilation and of volume transports at specific locations are combined with the dynamical balances in order to infer the basin-scale flow. The inferred flow displays the western boundary current and coherent structures in the abyssal interior with low statistical significance. In a second inversion, the flow is further constrained by the ^{230}Th measurements and the condition that ^{230}Th divergence by the flow field and particle sinking must be locally balanced by ^{230}Th production from ^{234}U decay. The addition of ^{230}Th leads to the estimation of a larger amplitude of the integrated meridional transports below 1000 m (by 2–9 Sv), where the range reflects the uncertainties in the large scale ^{230}Th distribution and in the radiochemical balance. This result is interpreted as a correction by ^{230}Th for the tendency of inverse geostrophic models to lead to the inference of a vanishing circulation when horizontal density gradients are insignificant.

1 Introduction

The abyssal circulation is notoriously difficult to study for obvious logistic but also physical reasons. Far from lateral boundaries and topographic passages (e.g., fracture zones) where currents can be coherent and intense, the dynamic method is relatively difficult to apply owing to the smallness of horizontal density gradients, whereas current meters and neutrally buoyant floats are often dominated by time-dependent motions (e.g., *Hogg and Owens* (1999)). Studies of the abyssal circulation rely also on the distribution of passive tracers that are either conservative (e.g., chlorofluorocarbons) or non-conservative (e.g., radiocarbon, tritium, oxygen, silicate). Interest in such tracers in physical oceanography stems primarily from the notion that their distribution represents a time integral of the circulation (e.g., *Wunsch and Grant* (1982)). Traditionally, the use of these distributions is qualitative, as it is limited to the provision of information about the geographical origin and pathways of water masses in the subthermocline region. More recently, attempts have been made to use the distribution of passive tracers in the inference of quantitative elements of the abyssal circulation (for a recent work see, e.g., *Vanicek and Siedler* (2002)).

In this paper we report on an attempt to extract quantitative information about the time mean flow in the abyssal North Atlantic basin from the distribution of thorium-230 (^{230}Th). Our motivation for considering this specific tracer is threefold. First, earlier studies claimed that ^{230}Th measurements in the North Atlantic contain information about the advection or 'ventilation' of deep waters in this basin (e.g., *Cochran et al.* (1987); *Moran et al.* (1997); *Vogler et al.* (1998); *Moran et al.* (2002)). The present investigation is a test of the claim based on a particular method of data analysis. Second, it has been hypothesized that the ^{230}Th activity in conjunction with the activity of another isotope (protactinium-231) in Atlantic sediments yields constraints on the circulation in the geological past (e.g., *Yu et al.* (1996)). In order to assess this hypothesis it is essential to understand the dynamical information that is provided by direct measurements of ^{230}Th and ^{231}Pa in the water column. Finally, the present work is motivated by the emerging international program GEOTRACES (*Anderson and Henderson*, 2005), which aims at improving our knowledge of the distribution of a variety of trace elements and their isotopes in the ocean – including ^{230}Th. This work attempts to determine the sufficiency of the current ^{230}Th data base from the viewpoint of its use in the inference of the circulation in the deep North Atlantic.

Our approach is based on the quantitative combination of ^{230}Th data with a model of the abyssal

circulation on the basis of an inverse method. Broadly, this method provides an estimate of the flow that is consistent in the least squares sense with the observations being considered and the model being postulated. Thus, neither the data nor the model balances are strictly imposed in the analysis, but they constrain the flow according to their respective estimated uncertainties. Here, we investigate the extent to which the consideration of ^{230}Th data complements inferences about the time mean flow in the abyssal North Atlantic made only from the density field and supplementary observations about volume fluxes at specific locations.

The paper is organized as follows. Section 2 provides a short review of the behavior of ^{230}Th in the ocean and reports new ^{230}Th measurements in the North Atlantic basin. A formal statement of the present problem of data–model combination is developed in section 3. The method used to extract dynamical information from the ^{230}Th distribution in the abyssal North Atlantic is described in section 4. An updated compilation of ^{230}Th measurements is presented, the model of the abyssal circulation is described, and the inverse method used to combine the ^{230}Th data and the model is identified. In section 5, this method is employed to investigate the effects of ^{230}Th data in the inference of the time mean flow in the basin. Emphasis is put on the estimation of the zonal and vertical integral of the meridional transport at different latitudes, i.e., on the lower branch of the meridional overturning circulation. The major results of this work are discussed in section 6. Conclusions and perspectives follow in section 7.

2 ^{230}Th in the North Atlantic

2.1 Behavior of ^{230}Th in the ocean

Thorium-230 is a naturally occurring radioisotope (half-life of $(75.69 \pm 0.23) \times 10^3$ yr; *Cheng et al.* (2000)) produced from the radioactive decay of uranium-234. The ^{234}U activity is about spatially uniform in the ocean, reaching ca. 2,940 dpm m^{-3} ('dpm' stands for 'disintegration per minute'; *Robinson et al.* (2004)). The rate of ^{230}Th production is

$$J_p = \lambda\, C(^{234}\mathrm{U}) \approx \frac{\ln 2}{76 \times 10^3} \times 2,940 = 2.7 \times 10^{-2} \text{ dpm m}^{-3} \text{ yr}^{-1}, \tag{1}$$

where λ is the constant of ^{230}Th radioactive decay and $C(^{234}\mathrm{U})$ is the ^{234}U activity in seawater. Unlike U, Th is rapidly removed from the water column by exchanges with particles sinking to the sediment (*Anderson et al.*, 1983b; *Anderson et al.*, 1983a; *Bacon*, 1988). A popular model describing this process

is the reversible exchange model (*Nozaki et al.*, 1981; *Bacon and Anderson*, 1982), whereby Th is continuously exchanged (via adsorption and desorption) with a single class of particles. The general governing equations for ^{230}Th activity in dissolved form (C_d) and particulate form (C_p) are then:

$$\frac{\partial C_d}{\partial t} + \mathbf{u} \cdot \nabla C_d = -\lambda C_d - J_e + J_p + \mathcal{D}_d, \tag{2}$$

$$\frac{\partial C_p}{\partial t} + \mathbf{u} \cdot \nabla C_p + w_s \frac{\partial C_p}{\partial z} = -\lambda C_p + J_e + \mathcal{D}_p. \tag{3}$$

Here t is time, $\mathbf{u} = (u, v, w)$ is the fluid velocity, w_s is the sinking velocity of the particles that participate in Th scavenging, ∇ is the gradient, J_e is the exchange between the dissolved and particulate forms, and $(\mathcal{D}_d, \mathcal{D}_p)$ represent the effects of diffusion. Summing (2–3) yields a governing equation for total ^{230}Th, $C = C_d + C_p$:

$$\frac{\partial C}{\partial t} + \mathbf{u} \cdot \nabla C + w_s \frac{\partial}{\partial z}(KC) = -\lambda C + J_p + \mathcal{D}. \tag{4}$$

where $K = C_p/C$ is a partitioning coefficient and $\mathcal{D} = \mathcal{D}_d + \mathcal{D}_p$. For example, precise measurements of C and C_d at a particular oceanic station lead to $K = 0.17 \pm 0.04$ ($n = 5$; *Roy-Barman et al.* (1996)). The term $-\lambda C$ in (4) can safely be omitted given the small ^{230}Th/^{234}U activity ratio in seawater (e.g., *Broecker and Peng* (1982)):

$$\frac{\lambda C}{J_p} = \frac{C}{C(^{234}\mathrm{U})} = \mathrm{O}\left(10^{-4}\right).$$

To isolate the scavenging effects consider the limit of a vanishing circulation and diffusion:

$$\frac{\partial C}{\partial t} + w_s \frac{\partial}{\partial z}(KC) = J_p. \tag{5}$$

Note that the omission of $(\mathbf{u}, \mathcal{D})$ is a very strong assumption, except perhaps for vertical advection: estimates of the vertical velocity (w) in the abyssal ocean of $\mathrm{O}(10^{-7}$–$10^{-6})$ m s^{-1} have been reported (e.g., *Olbers et al.* (1985); *Morris et al.* (2001)), whereas estimates of w_s are in the range $(3$–$9)\times10^2$ m yr^{-1} or $(1$–$3)\times10^{-5}$ m s^{-1} (*Krishnaswami et al.*, 1976; *Krishnaswami et al.*, 1981; *Rutgers van der Loeff and Berger*, 1993; *Scholten et al.*, 1995). Thus, the vertical advection of ^{230}Th appears generally small compared its vertical transport by sinking particles. Equation (5) is solved by assuming zero initial ^{230}Th at all depths and zero ^{230}Th at the sea surface at all times. Note that the latter condition is only an approximation as ^{230}Th is always present in detectable amount in surface waters. For constant (w_s, K, J_p), the solution of (5) with these conditions is

$$C(z,t) = \frac{J_p}{w_*}\left(z - (z - w_* t)\,\mathcal{H}[z - w_* t]\right), \tag{6}$$

where $w_* = w_s K$ is a pseudo sinking velocity and $\mathcal{H}[\cdot]$ is the unit step function, i.e.,

$$\begin{aligned} &= 0 \ (x < 0), \\ \mathcal{H}[x] &= \frac{1}{2} \ (x = 0), \\ &= 1 \ (x > 0). \end{aligned}$$

Thus, in the absence of advection and diffusion, the activity of ^{230}Th would increase linearly in time at a rate J_p to the steady state value $C(z) = (J_p/w_*)z$. If the time to steady state is short, the distribution of ^{230}Th would largely reflect the reversible exchange with particles, whereas if it is long, the distribution would be influenced by processes that are disregarded in (5), such as advection and diffusion. Assuming $w_* = w_s K = 600 \times 0.17 = 102$ m yr^{-1}, it would take the ^{230}Th activity $z/w_* = 10$ yr (49 yr) to reach the steady value at $z = 1000$ m (5000 m). The steady state value would be reached first in shallow water and then in deep water. Note that at steady state the total ^{230}Th activity increases linearly with depth, which is consistent with observations in some oceanic regions (e.g., *Roy-Barman et al.* (1996)).

2.2 New ^{230}Th data for the North Atlantic

Measurements of ^{230}Th in the North Atlantic show significant departures from a linear distribution, which have been interpreted in terms of advection or ventilation (e.g., *Cochran et al.* (1987); *Moran et al.* (1997); *Vogler et al.* (1998); *Moran et al.* (2002)). We have extended significantly the ^{230}Th data base in this basin (Figure 1). Only a brief description of the new ^{230}Th measurements is given here; the methods of data collection and analysis are described in the appendix. Consider a collection of ^{230}Th profiles from very distant stations in the basin (Figure 2). The activity values exhibit generally a similar increase with depth in the upper ~ 1000 m of the water column. Thus, a process common to all locations – most probably a reversible exchange with sinking particles – seems to dominate the behavior of the tracer in this depth interval. In contrast, the activity values at depth larger than ca. 1000 m show very large geographic variations. A question of preeminent interest is whether these variations result from the effects of the circulation – by preventing the slow attainment to steady state with respect to particle exchange in deep water – and hence contain information about the abyssal flow in the basin.

Note that other processes have been identified as potential influences on the ^{230}Th distribution in the North Atlantic. It was suggested that low ^{230}Th activities observed at some stations could result from a local enhancement of scavenging (*Mangini and Key*, 1983; *Vogler et al.*, 1998). More generally, the

chemical composition of particles could influence the ^{230}Th distribution (e.g., *Chase et al.* (2002); *Guo et al.* (2002); *Roy-Barman et al.* (2005)). Depletion of Th near the seafloor (bottom scavenging; e.g., *Bacon and Rutgers van der Loeff* (1989)) and enhanced Th scavenging at the ocean margins (boundary scavenging; e.g., *Anderson et al.* (1994)) have been reported in the North Atlantic, which may be due to the large concentration and/or the chemical composition of the particles that are locally present. Thus, our understanding of ^{230}Th behavior in the ocean is still incomplete (for a recent review of Th chemistry in seawater, see *Santschi et al.* (2006)).

3 Statement of the Problem

In spite of the present incomplete understanding of ^{230}Th in the ocean, legitimate questions arise: What do the existing measurements of ^{230}Th activity tell us about the abyssal circulation in the North Atlantic basin? Can a large-scale circulation scheme compatible with geostrophic dynamics, hydrographic data, and ^{230}Th measurements be found? Will the hydrography and ^{230}Th data be complementary so that the consideration of the radiochemical measurements will improve the estimate of the abyssal circulation? Here these questions are addressed by combining ^{230}Th data with a finite-difference model of the abyssal circulation using an inverse method.

Our problem is stated as follows. Consider a state vector $\mathbf{x}$, whose elements describe the state of the deep North Atlantic in terms of the model. In our case the elements of $\mathbf{x}$ are the seawater density, the three components of transport (in units of Sv $\equiv 10^6$ m^3 s^{-1}), and the ^{230}Th activity at different locations of the model grid. Consider an a priori (before inversion) estimate of $\mathbf{x}$, $\mathbf{x}_o$, and its error covariance matrix, $\mathbf{C}_o \equiv E(\mathbf{x}-\mathbf{x}_o)(\mathbf{x}-\mathbf{x}_o)^{\mathrm{T}}$, where E is the expected value (mean) and $^{\mathrm{T}}$ denotes the transpose (the diagonal elements of $\mathbf{C}_o$ are the variances of the elements of $\mathbf{x}_o$, whereas the off-diagonal elements of $\mathbf{C}_o$ are the covariances between these elements). Typically, $\mathbf{x}_o$ includes observational estimates and $\mathbf{C}_o$ includes their estimated (co)variances. Finally, consider a set of relationships between the different elements of $\mathbf{x}$, $\mathbf{f}(\mathbf{x}) = \mathbf{0}$, and its error covariance matrix, $\mathbf{C}_f$. Here these relationships are formal constraints on the time-mean flow (e.g., this flow should be mass-conserving and approximately in geostrophic balance). Our problem is to produce an estimate of $\mathbf{x}$ that is consistent with the observation $\mathbf{x}_o$ and the formal constraints $\mathbf{f}(\mathbf{x}) = \mathbf{0}$, given their respective uncertainties $\mathbf{C}_o$ and $\mathbf{C}_f$. It corresponds to minimizing a cost

function (e.g., *Mercier* (1986)):

$$I = (\mathbf{x} - \mathbf{x}_o)^{\mathrm{T}}\, \mathbf{C}_o^{-1}\, (\mathbf{x} - \mathbf{x}_o) + \mathbf{f}(\mathbf{x})^{\mathrm{T}} \mathbf{C}_f^{-1} \mathbf{f}(\mathbf{x}). \tag{7}$$

Thus, the error covariance matrices play the role of weighting factors in the minimization. Assuming uncorrelated errors (diagonal matrices), a particular observation or constraint with a large uncertainty has a relatively small influence on the solution.

4 Method

In this section we describe our approach to evaluate the dynamical information contained in measurements of ^{230}Th activity in the abyssal North Atlantic. Two types of inversions are conducted: the inversion of density data and the simultaneous inversion of density and ^{230}Th data. Comparing results from both inversions gives insight into the additional information brought by the radiochemical measurements. In the following, the observations used to constrain the flow are described, the formal constraints $\mathbf{f}(\mathbf{x}) = \mathbf{0}$ are presented, and the method used for minimizing the cost I is identified.

4.1 Distribution of ^{230}Th

The ^{230}Th values included in $\mathbf{x}_o$ are total ^{230}Th activities in units of dpm m^{-3}. A compilation of ^{230}Th measurements between 0° and 60°N in the Atlantic is presented (Table 1; Figure 1). Different investigators use different units for the ^{230}Th activity (e.g., dpm m^{-3}, dpm (10^3 kg)$^{-1}$, fg kg^{-1}, etc.). Here all ^{230}Th activities are expressed in dpm m^{-3} assuming a seawater density of 1028 kg m^{-3} and the conversion 1 fg ^{230}Th $\equiv 4.56 \cdot 10^{-5}$ dpm. According to our compilation, dissolved (particulate) ^{230}Th has been determined at 21 (8) stations. For some stations (16 stations), total ^{230}Th has been determined directly (measurements on unfiltered water samples). When both dissolved and particulate ^{230}Th have been determined but not total ^{230}Th, the total ^{230}Th is taken as the sum of both forms. When only dissolved ^{230}Th has been measured, the total ^{230}Th is estimated from dissolved ^{230}Th and the mean value of the partitioning coefficients determined from paired measurements of dissolved and particulate ^{230}Th that are available at 8 stations (mean $K = 0.15$ with a standard error of 0.01; $n = 75$). With this approach an estimate of total ^{230}Th is available at 341 data locations (longitude, latitude, and depth) distributed among 37 stations (Figure 1).

The entries along the diagonal of $\mathbf{C}_o$ are variances (standard deviations squared) of total ^{230}Th in units of (dpm m^{-3})^2. We attempt to produce homogeneous estimates of the standard deviations (σ_{Th} hereafter) on the basis of the errors reported in the original publications (Table 1). When total ^{230}Th has been directly measured, σ_{Th} is the error estimate reported in the original publication. When both dissolved and particulate ^{230}Th are available, σ_{Th} is taken as the square root of the quadratic sum of the errors in dissolved and particulate ^{230}Th assuming no correlation between these errors. When total ^{230}Th is estimated from dissolved ^{230}Th and the mean $K = 0.15$, σ_{Th} is taken as the square root of the quadratic sum of the errors in dissolved ^{230}Th and in the partitioning coefficient, assuming no correlation between these errors. In this case the error for K is taken as the standard deviation of $0.01 \times \sqrt{75} = 0.10$.

Note that we suppose in this work that (i) ^{230}Th data originating from different laboratories and/or generated by different investigators could be used to constitute a homogeneous data set; and (ii) ^{230}Th data collected at different times could be considered as synoptic. Whereas assumptions (i–ii) seem necessary to make any progress possible, it should be mentioned that these are working hypotheses that will need to be tested through intercalibration efforts and a more extensive data set.

The ^{230}Th data base provides guidance for a sensible choice of the model domain (Figure 1). The chosen domain extends from 10.5°N–49.5°N in latitude and 1000–5000 m in depth, with a resolution of 3° × 3° × 1000 m. A much higher resolution is not warranted given the paucity of ^{230}Th data, whereas a much lower resolution would worsen the representation of ^{230}Th differences observed in the basin (e.g., Figure 2). The chosen resolution appears therefore as a reasonable compromise. The restriction of the domain to depths larger than 1000 m is justified by the fact that ^{230}Th shows small geographic variations in the upper part of the water column (e.g., Figure 2). The bathymetry at the model resolution is obtained by averaging depth values of ETOPO5 (available at 5' resolution).

Our method of data analysis assumes the availability of an estimate of total ^{230}Th and of its variance at each model grid point; these gridded estimates are the values to be included in $\mathbf{x}_o$ and $\mathbf{C}_o$, respectively. An objective mapping (e.g., *Bretherton et al.* (1976)) is used to produce an estimate of total ^{230}Th and of its variance at the regularly spaced model grid points from the ^{230}Th measurements and their errors at the irregularly spaced data locations. Because the ^{230}Th values in the upper 1000 m of the water column tend to be systematically lower than below (section 2), these values are not considered in objective mapping so as not to bias the ^{230}Th estimates at the grid points (at $z \geq 1000$ m). Hence, the

number of ^{230}Th data points effectively used in objective mapping amounts to 235. Details about the mapping are reported in section 5.2.1.

4.2 Distribution of density

The distribution of density is derived from the hydrographic data set *HydroBase* (*Lozier et al.*, 1995; *Curry*, 2001). This data set includes compilations of in situ temperature (T) and salinity (S) from the World Ocean Database 1998, the Hydrographic Program of the World Ocean Circulation Experiment, and a few other archives. The value of in situ density (ρ) at a model grid point is obtained by subsampling the climatologic distributions of the annual mean (T, S) at depths 1000, 2000, 3000, 4000, and 5000 m produced on a grid with $1^\circ \times 1^\circ$ resolution. When a model grid point does not coincide with a point of the climatologic grid, the climatologic (T, S) values at the closest point are selected. The ρ values at model grid points are computed from T, S, and pressure using EOS-80.

The density error at a given model grid point is obtained by subsampling the distributions of the standard deviations of (T, S) at depths 1000, 2000, 3000, 4000, and 5000 m produced from *HydroBase*. These deviations reflect the variability in each 1° square of the climatologic grid. Again, if the model grid point does not coincide with a point of the climatologic grid, the climatologic deviations at the closest point are chosen. To propagate the (T, S) deviations on the density error we use a linear equation of state with depth-dependent derivatives $\partial\rho/\partial T$ and $\partial\rho/\partial S$ (Table 2), neglect the pressure error, and assume zero correlation between the (T, S) deviations.

4.3 Model constraints

We request that our circulation estimates be consistent with a simplified model of the circulation and of the behavior of ^{230}Th in the abyssal region. The motive for this approach is that the model equations are not perfectly satisfied in our analysis. Our model includes two components: a physical component and a radiochemical component.

4.3.1 Physical component

The physical component is a model of the time mean flow based on the following approximations: the fluid is incompressible and Boussinesq, and the flow is geostrophic, hydrostatic, and adiabatic (e.g.,

Mercier (1989); *Martel and Wunsch* (1993); *Mercier et al.* (1993); *Vanicek and Siedler* (2002)). The dynamical equations are discretized on a regular grid, where grid boxes have a longitudinal size $\Delta\phi = 3°$, a latitudinal size $\Delta\theta = 3°$, and a vertical size $\Delta z = 1000$ m. The transport components (U, V, W) are defined at the box faces, whereas $(\rho, {}^{230}\mathrm{Th})$ are carried by the box corners (e.g., by the point with coordinates i, j, k). The difference form of the mass conservation equation is

$$U_{i+1,j+\frac{1}{2},k+\frac{1}{2}} - U_{i,j+\frac{1}{2},k+\frac{1}{2}} + V_{i+\frac{1}{2},j+1,k+\frac{1}{2}} - V_{i+\frac{1}{2},j,k+\frac{1}{2}} + W_{i+\frac{1}{2},j+\frac{1}{2},k+1} - W_{i+\frac{1}{2},j+\frac{1}{2},k} = 0. \tag{8}$$

The difference analogues of the thermal wind relations are

$$V_{i+\frac{1}{2},j,k+\frac{1}{2}} - V_{i+\frac{1}{2},j,k-\frac{1}{2}} + \frac{g\Delta z^2}{2\Omega\rho_0}\frac{\rho_{i+1,j,k} - \rho_{i,j,k}}{\sin\theta_j} = 0, \tag{9}$$

$$U_{i,j+\frac{1}{2},k+\frac{1}{2}} - U_{i,j+\frac{1}{2},k-\frac{1}{2}} + \frac{g\Delta z^2\Delta\theta}{2\Omega\rho_0}\frac{\rho_{i,j+1,k} - \rho_{i,j,k}}{\Delta(\cos\theta)|_j^{j+1}} = 0. \tag{10}$$

Here $g = 9.81$ m s^{-2} is the acceleration of gravity, $\Omega = 7.29 \times 10^{-5}$ s^{-1} is the angular velocity of earth rotation, $\rho_0 = 1028$ kg m^{-3} is a reference density, and $\Delta(\cos\theta)|_j^{j+1} \equiv \cos\theta_{j+1} - \cos\theta_j$. The difference form of the linear vorticity equation, $(a\tan\theta)^{-1}v = \partial w/\partial z$, where v (w) is the meridional (vertical) velocity, is

$$\frac{1}{2a}\left(\frac{v_{i+\frac{1}{2},j,k+\frac{1}{2}}}{\tan\theta_j} + \frac{v_{i+\frac{1}{2},j+1,k+\frac{1}{2}}}{\tan\theta_{j+1}}\right) = \frac{w_{i+\frac{1}{2},j+\frac{1}{2},k+1} - w_{i+\frac{1}{2},j+\frac{1}{2},k}}{\Delta z}.$$

Multiplying by the grid box volume $\Delta\mathcal{V} = a^2\cos\theta\Delta\theta\Delta\phi\Delta z = a^2\Delta(\sin\theta)\Delta\phi\Delta z$ gives

$$\frac{a\Delta(\sin\theta)|_j^{j+1}\Delta\phi\Delta z}{2}\left(\frac{v_{i+\frac{1}{2},j,k+\frac{1}{2}}}{\tan\theta_j} + \frac{v_{i+\frac{1}{2},j+1,k+\frac{1}{2}}}{\tan\theta_{j+1}}\right) = a^2\Delta(\sin\theta)|_j^{j+1}\Delta\phi\left(w_{i+\frac{1}{2},j+\frac{1}{2},k+1} - w_{i+\frac{1}{2},j+\frac{1}{2},k}\right).$$

In terms of volume fluxes (transports),

$$\frac{\Delta(\sin\theta)|_j^{j+1}}{2}\left(\frac{V_{i+\frac{1}{2},j,k+\frac{1}{2}}}{\sin\theta_j} + \frac{V_{i+\frac{1}{2},j+1,k+\frac{1}{2}}}{\sin\theta_{j+1}}\right) - W_{i+\frac{1}{2},j+\frac{1}{2},k+1} + W_{i+\frac{1}{2},j+\frac{1}{2},k} = 0. \tag{11}$$

Finally, the difference form of the density equation is

$$\begin{aligned} U_{i+1,j+\frac{1}{2},k+\frac{1}{2}}\bar{\rho'}_{i+1} - U_{i,j+\frac{1}{2},k+\frac{1}{2}}\bar{\rho'}_i &+ \\ V_{i+\frac{1}{2},j+1,k+\frac{1}{2}}\bar{\rho'}_{j+1} - V_{i+\frac{1}{2},j,k+\frac{1}{2}}\bar{\rho'}_j &+ \\ W_{i+\frac{1}{2},j+\frac{1}{2},k+1}\bar{\rho'}_{k+1} - W_{i+\frac{1}{2},j+\frac{1}{2},k}\bar{\rho'}_k &= 0. \end{aligned} \tag{12}$$

Here $\rho' = \rho - \bar{\rho}$ is the anomaly of in situ density ($\bar{\rho} = 1041$ kg m^{-3} is a mean value) and $\bar{\rho'}$ is the average of the four anomalies at the corresponding box face, e.g.,

$$\bar{\rho'}_i = \frac{1}{4}\left(\rho'_{i,j,k} + \rho'_{i,j+1,k} + \rho'_{i,j+1,k+1} + \rho'_{i,j,k+1}\right).$$

The errors in the dynamical balances (8–12) stem from missing physics and the discretization. A small standard deviation of 0.01 Sv is used for (8) in order to ensure that the circulation schemes obtained by inversion are mass-conserving (more exactly, volume-conserving) to a very good approximation. A value of 1 Sv is assumed for the standard deviations for (9–11), which should partly account for ageostrophic effects. Note that (11) is not imposed for grid boxes in the upper three model layers and along the western boundary, i.e., at locations where the constraint of a strong western boundary current is imposed (section 4.4). Finally, the standard deviation for (12) is fixed at 10^{-2} Sv kg m^{-3}, which should allow at least partly for diabatic and compression effects.

4.3.2 Radiochemical component

The radiochemical component is a description of the behavior of ^{230}Th in the ocean based on several assumptions. First, we follow the reversible exchange model by assuming a single class of particles; the general governing equation for total ^{230}Th is then (4). Second, we assume steady state ($\partial C/\partial t = 0$). This assumption is guided by our working hypothesis that the ^{230}Th data can be regarded as synoptic, thereby omitting any time-dependency in the analysis. Third, the effects of radioactive decay ($-\lambda C$) and diffusion ($\mathcal{D}$) are neglected. Finally, we omit the term $w_s C \partial K/\partial z$, so that $w_s \partial(KC)/\partial z = w_* \partial C/\partial z$. Insight into this assumption is obtained by estimating the gradient $\partial K/\partial z$ that would be required for the neglected term to be comparable to the production term J_p. The required gradient $\partial K/\partial z = J_p/(w_s C)$ is estimated to lie in the range 0.07–0.20 km^{-1}, which is generally larger than the gradients observed in situ (Figure 3). Although the comparison is by no means conclusive (e.g., some K values near the seafloor are relatively high – owing perhaps to bottom scavenging – which produces large local gradients $\partial K/\partial z$), it does suggest that the effect of vertical changes in the partitioning coefficient could be omitted to lowest order to describe the effects of particle scavenging in the abyssal region. Under these various assumptions, the governing equation for total ^{230}Th can be written as

$$\nabla \cdot (\mathbf{u}_e C) = J_p.$$

Here $\mathbf{u}_e = (u, v, w_e)$, where $w_e = w + w_*$ is an effective vertical velocity. The divergence of the total ^{230}Th flux by the flow field and particle sinking is balanced by ^{230}Th production from ^{234}U decay. The difference analogue of the latter equation is

$$U_{i+1,j+\frac{1}{2},k+\frac{1}{2}} \bar{C}_{i+1} - U_{i,j+\frac{1}{2},k+\frac{1}{2}} \bar{C}_i \quad + \tag{13}$$

$$V_{i+\frac{1}{2},j+1,k+\frac{1}{2}}\bar{C}_{j+1} - V_{i+\frac{1}{2},j,k+\frac{1}{2}}\bar{C}_j \quad +$$

$$W_{i+\frac{1}{2},j+\frac{1}{2},k+1}\bar{C}_{k+1} - W_{i+\frac{1}{2},j+\frac{1}{2},k}\bar{C}_k \quad +$$

$$W_{e,i+\frac{1}{2},j+\frac{1}{2},k+1}\bar{C}_{k+1} - W_{e,i+\frac{1}{2},j+\frac{1}{2},k}\bar{C}_k \quad - \quad J_p\Delta\mathcal{V} = 0.$$

Here $W_e = a^2\Delta(\sin\theta)\Delta\phi w_e$ and $\bar{C}$ is the average of the four ^{230}Th values at the box face.

The radiochemical balance (13) contains the pseudo sinking velocity $w_* = w_s K$, which describes the overall efficacy of ^{230}Th scavenging by sinking particles. To estimate w_* we consider vertical profiles of dissolved ^{230}Th (Figure 2). As noted earlier, these profiles share a common trend in the upper $\sim$ 1000 m. A linear regression of the data for the upper 1000 m yields a slope $b = (2.0 \pm 0.1) \times 10^{-4}$ dpm m^{-4} ($r = 0.95$; $n = 46$). According to the reversible exchange model, the slope has the following interpretation,

$$b = \frac{J_p\,(1-K)}{w_*}.$$

Here it was assumed that K is vertically uniform in the upper 1000 m, which does not seem unreasonable in the light of the few estimates (Figure 3). The above equation can be used to estimate w_* and its uncertainty. Assuming $J_p = 2.7 \times 10^{-2}$ dpm m^{-3} yr^{-1}, $K = 0.15$, and $b = 2.0 \times 10^{-4}$ dpm m^{-4}, we obtain $w_* = 115$ m yr^{-1}. The uncertainty in this value is estimated assuming a negligible error for J_p and uncorrelated errors of 0.10 for K and 0.1×10^{-4} dpm m^{-4} for b. Hence we obtain $w_* = 115 \pm 14$ m yr^{-1}, i.e., a relative precision of 12%. This value is used for w_* in our inversions, assuming that it is also representative of scavenging at depth larger than 1000 m.

The error in (13) stems from various sources, such as the consideration of a single class of particles, the omission of terms such as diffusion and $w_s C\partial K/\partial z$, our assumption that w_* is spatially uniform, and the discretization. Thus, (13) should only be imposed mildly. Here we accept solutions characterized by imbalances in (13) that are on the same order as the production term. The rate of ^{230}Th production by ^{234}U decay integrated over a volume of 3°$\times$ 3°$\times$ 1000 m is $\sim 3 \times 10^{12}$ dpm yr^{-1}, which corresponds to a value of $\sim$ 0.1 Sv dpm m^{-3}. Unless stipulated otherwise, the standard deviation for (13) is fixed at this value.

4.4 Kinematical constraints

To further constrain the circulation we rely on observational estimates of volume transport at specific locations in the abyssal North Atlantic. Our motivation for doing this is that these fluxes would otherwise be poorly represented or not represented at all given the coarse resolution of the model. Most notably, a density field with a resolution of $3^\circ \times 3^\circ$ cannot capture accurately the strong horizontal gradients across the western boundary, which would lead to a serious underestimation of the flow amplitudes in this region.

Schmitz (1996) proposed a 'consensus' regarding several elements of the North Atlantic circulation. We rely on his circulation scheme for the North Atlantic Deep Water (NADW) (*Schmitz* (1996); p. 93), which is largely based on the synthesis of *Schmitz and McCartney* (1993). According to this scheme the western boundary south of $\sim 20^\circ$N carries a southward volume flux of 18 Sv in amplitude; more to the north the NADW flux is composed of two branches, one along the western boundary (12 Sv) and another one located in the interior of the western basin (6 Sv). Here we assume that the western boundary between 10.5°N and 49.5°N and between 1000 and 4000 m carries a volume flux of 18 Sv. The confinement of this constraint to between 1000 and 4000 m is based on the identification of the deep western boundary current (DWBC) approximately in this depth interval from a variety of hydrographic and chemical measurements (e.g., *Fine and Molinari* (1988); *Pickart* (1992); *Molinari et al.* (1992)). Note that we do not distinguish between the two branches that contribute to the NADW flux, as postulated by *Schmitz* (1996) (p. 93). We assume an uncertainty (one standard deviation) of 3 Sv for this flux.

Stephens and Marshall (2000) estimated the pathways of Antarctic Bottom Water (AABW) in the Atlantic. We assume, at the southern boundary of the model domain (10.5°N) and in the deepest model layer (4000–5000 m), a northward flux of 2 Sv both on the western side of the ridge (between 45.5°W and 48.5°W) and on the eastern side of the ridge (between 36.5°W and 39.5°W), consistent with their circulation scheme (*Stephens and Marshall* (2000); Fig. 1). We assume an uncertainty of 0.5 Sv in this value.

Finally, the westward flux of Mediterranean Outflow Water (MOW) into the Atlantic basin has been estimated to be –2.2 Sv by *Ochoa and Bray* (1991) and –1.9 Sv by *Baringer and Price* (1997). We assume a westward flux of MOW of -2.0 Sv at the eastern edge of the model domain (9.5°W) between 34.5°N

and 37.5°N and in the 1000–2000 m layer, which is in the range of these observational estimates. The uncertainty of this flux is fixed at 0.3 Sv, which is equal to the range of these estimates.

4.5 Inverse method

The prior estimate $\mathbf{x}_o$ (with uncertainty $\mathbf{C}_o$) and the constraints $\mathbf{f}(\mathbf{x}) = \mathbf{0}$ (with uncertainty $\mathbf{C}_f$) described in the previous sections are combined; i.e., a minimum of the cost I (7) is sought. To find a minimum we use the algorithm of total inversion of *Tarantola and Valette* (1982), as modified by *Mercier* (1986) to account for imperfect model constraints (the algorithm is iterative). The uncertainty of the solution $\tilde{\mathbf{x}}$, $\mathbf{C} \equiv E(\mathbf{x} - \tilde{\mathbf{x}})(\mathbf{x} - \tilde{\mathbf{x}})^{\mathrm{T}}$, is calculated from an analogy with recursive weigthed least squares (*Wunsch* (2006); p. 137).

5 Results

In this section we report the results from two different inversions. First, only the density data are inverted, i.e., the density distribution derived from *HydroBase* is combined with the dynamical constraints (8–12) and the kinematical constraints. The role of this inversion is not to supersede earlier inferences of the flow in the abyssal North Atlantic based, e.g., on models with higher resolution (e.g., *Martel and Wunsch* (1993)). Its primary aims are (i) to test the inverse method without the additional complexities introduced by a passive tracer; and (ii) to serve as a reference against which the effects of considering in addition ^{230}Th data in the inferential process could be evaluated. Second, both density and ^{230}Th data are inverted, i.e., the density distribution derived from *HydroBase* and the ^{230}Th distribution obtained by objective mapping are combined simultaneously with the model constraints (8–13) and the kinematical constraints. Comparing results obtained from the two inversions will allow us to identify the influence of ^{230}Th measurements on the estimation of the time mean flow in the abyssal basin.

5.1 Inversion of density data

5.1.1 Prior state and uncertainties

Here the state $\mathbf{x}$ includes the density and the three components of transport (U, V, W) at different locations of the model grid. The prior $\mathbf{x}_o$ is constructed as follows. The density distribution comes from *HydroBase*

(section 4.2). The horizontal transports (U, V) are either (i) diagnosed from this distribution and the thermal wind (9–10) assuming an arbitrary level of no motion at a depth of 3000 m or the seafloor if shallower; or (ii) prescribed according to observational estimates. Option (ii) is used only along the western boundary and at the inflows of AABW and MOW into the basin (section 4.4). The transports along the western boundary between 1000 and 4000 m (three upper model layers) are assigned a prior value of –6 Sv (for westward and southward transports) or +6 Sv (eastward transport). Thus, the integrated volume flux of 18 Sv in amplitude (section 4.4) is a priori partitioned equally among the three layers. The vertical transports W are deduced by continuity (8) assuming no normal flow at the rigid boundaries (i.e., at the bottom and at most of the lateral boundaries).

The error covariance matrices $\mathbf{C}_o$ and $\mathbf{C}_f$ are taken as diagonal. The diagonal elements of $\mathbf{C}_o$ are the variances of the density and transport values assumed in $\mathbf{x}_o$. The standard deviations for ρ are obtained from *HydroBase* (section 4.2). The standard deviations for (U, V) are equal to 3 Sv – a relatively large value motivated by the assumption about a level of no motion. The same value is used for the standard deviations of (U, V) along the western boundary, whereas lower values are used for the inflows of AABW and MOW (section 4.4). The standard deviation for W is taken as 3 Sv everywhere. The diagonal elements of $\mathbf{C}_f$ are the variances for the difference forms (8–12) and the kinematical constraints along the western boundary (the variances for the other kinematical constraints are present in $\mathbf{C}_o$). These variances have been specified in sections 4.3.1 and 4.4.

In summary, the prior state $\mathbf{x}_o$ satisfies the mass conservation and the thermal wind (except for (9–10) along the western boundary and at locations of inflows of AABW and MOW). It is used to initialize the inversion. In the course of the inversion the state should adjust so as to also satisfy the linear vorticity balance and the density equation. The number of adjustable variables (number of elements of $\mathbf{x}$) amounts to 3389, and the number of formal constraints (dynamical and kinematical constraints in $\mathbf{f}$) is 3089.

5.1.2 Reference inversion

We discuss the results obtained from the inversion of density data (hereafter, the reference inversion). The cost function I decreases by 6 orders of magnitude in 3 iterations and exhibits then minor changes (not shown). We consider as the solution $\tilde{\mathbf{x}}$ the state estimate after convergence of the total cost (after 4 iterations). In order to explore the uniqueness of this solution we initialize the inversion from a different

position in the state space. Each element of the initial state is perturbed by a gaussian deviate with zero mean and unit variance, i.e., each element is initially equal to $x_{oi} + \delta\sqrt{C_{oi}}$, where $E(\delta) = 0$ and $E(\delta^2) = 1$. In this case the total cost converges after 5 iterations (not shown). After convergence the state elements are almost identical to those obtained from the unperturbed initial state (e.g., the r.m.s. difference for each transport component $< 10^{-4}$ Sv), suggesting that the solution is stable.

We then verify that the solution is consistent with the prior estimates and the formal constraints, given their respective uncertainties. The diagnostics are the normalized residuals, i.e., the square root of each term of the quadratic forms $(\tilde{\mathbf{x}} - \mathbf{x}_o)^{\mathrm{T}}\mathbf{C}_o^{-1}(\tilde{\mathbf{x}} - \mathbf{x}_o)$ and $\mathbf{f}(\tilde{\mathbf{x}})^{\mathrm{T}}\mathbf{C}_f^{-1}\mathbf{f}(\tilde{\mathbf{x}})$. A posterior estimate is regarded as compatible with its prior estimate or a constraint is deemed satisfied, if the corresponding normalized residual < 2 in absolute magnitude – a criterion that gives a 95% confidence level in a gaussian framework. We find that most residuals comply with this criterion: the fraction of normalized residuals ≥ 2 in absolute magnitude amounts to $(0.00, 0.01, 0.00, 0.06)$ for (ρ, U, V, W) (Figure 4a), to 0.09 for the kinematical constraints along the western boundary (open circles in Figure 4b), and to 0.00 for the model equations (9–13) (solid circles in Figure 4b). The density and transport fields assumed in $\mathbf{x}_o$ have been slightly adjusted during the inversion so as to satisfy the linear vorticity balance and the density equation (Figure 4a). Thus the inversion brings into consistency the prior information with the full dynamics, but it also detects the information that is not internally compatible. For example, some of the prior estimates of W and some of the integrated transports along the western boundary have too large residuals according to our criterion. We anticipate that the incompatibility for the integrated transports results from the coarse resolution employed here: a transport amplitude of 18 ± 3 Sv might not be consistent with the integrated transport implied by the horizontal density gradients at some locations. Nonetheless, most of the integrated fluxes along the western boundary (21 over 23) do show consistency with the full dynamics (Figure 4b). Thus, the circulation scheme obtained by inverting the density data fulfills generally both the prior estimates and the postulated constraints.

We now consider some elements of the circulation scheme. The zonal and vertical integral (below a depth of 1000 m) of the meridional transport varies with latitude, ranging from -16.8 ± 3.4 Sv to -13.9 ± 3.4 Sv. The values south of 34.5°N have larger amplitudes than north of this latitude because of the inflow of MOW that recirculates primarily to the south. South and north of 34.5°N, the integrated transports are very similar owing to the relatively small vertical velocities at $z = 1000$ m estimated a posteriori (the

average velocities at $z = 1000$, 2000, 3000, and 4000 m have amplitudes ranging from 0.3×10^{-7} m s^{-1} to 0.4×10^{-7} m s^{-1}). Note the relatively small uncertainties in the integrated transports compared to their amplitudes.

We compare the integrated meridional transports with the few estimates based on transatlantic sections (Figure 5), although agreement with these estimates should not be necessarily expected (e.g., the hydrographic data used here were collected over decades, whereas those obtained during a transatlantic section span typically a period of $\sim$ 1 month). *Roemmich and Wunsch* (1985) (their Table 1) estimated volume fluxes from –20.9 to –16.8 Sv across 25°N and from –19.4 to –12.9 Sv across 36°N beneath $\sigma_2 = 36.82$ (i.e., below about $z = 1300$ m), where the ranges reflect different sections (taken in 1957, 1959, and 1981) and different assumptions in the transport estimation. *Bryden et al.* (2005) (their Table 1) reported fluxes from –22.9 to –14.8 Sv across 25°N below $z = 1000$ m; the range reflects sections completed in 1957, 1981, 1992, 1998, and 2004. The range of transport values at 25°N from both studies encompasses the estimate of subthermocline flux (below $\sigma_\theta = 27.3$) of –17.6 Sv reported in the synthesis of *Talley* (2003) (her Table 7). We find that most estimates based on transatlantic sections agree with the integrated meridional transports inferred here, considering only the uncertainties in the latter (Figure 5).

We then consider the horizontal circulation in the four abyssal layers. The most salient features for the depth-integrated flow between 1000 and 4000 m are the large volume fluxes along the western boundary (Figure 6a). Several coherent structures are also suggested in the interior. In the layer between 2000 and 3000 m a conspicuous feature is the eastward flow in the southeastern part of the basin (Figure 7a). Between 3000 and 4000 m a countercurrent is present seaward of the western boundary current in the northern half of the basin, and an anticyclonic circulation takes places in the southern half of the eastern basin (Figure 8a). The deepest layer, between 4000 and 5000 m, exhibits several features, e.g., an outflow and an inflow west of the ridge at the southern edge of the domain, a cyclonic circulation in the northern part of the western basin, and, as in the overlying layer, an anticlyclonic circulation in the southern half of the eastern basin (Figure 9a). Note that, in contrast to the volume fluxes along the western boundary, which are relatively well determined (Figure 6b), the uncertainties of the individual transports in the interior are comparable to the transport amplitudes (Figures 7–9).

5.1.3 Comparison with earlier circulation schemes

A short comparison between our circulation scheme (Figures 6–9) and earlier quantitative inferences of the abyssal flow in the North Atlantic is probably in order. Note that different circulation estimates should not necessarily agree: for example, investigators used different hydrographic data and/or formal constraints to estimate the flow. The use of varying horizontal and vertical resolutions makes also delicate the comparison of circulation schemes inferred in different studies. We consider the circulation estimates from a sample of studies that encompass a range in observations, formal constraints, and inverse techniques (*Wunsch*, 1978; *Wunsch and Grant*, 1982; *Olbers et al.*, 1985; *Mercier et al.*, 1993; *Martel and Wunsch*, 1993). A western boundary current is a common feature of most of these estimates (here the current is imposed as a kinematical constraint). In contrast, discrepancies exist regarding flow structures in the interior (e.g., *Olbers et al.* (1985); *Martel and Wunsch* (1993)). A structure that shares some similarity with results from earlier studies is the recirculation at the southern edge of the westward flowing boundary current near 40°N (*Wunsch*, 1978; *Wunsch and Grant*, 1982). This recirculation is present both between 1000 and 4000 m (Figure 6a) and between 4000 and 5000 m (Figure 9a). Its association with the 'Northern Recirculation Gyre' located offshore of the western boundary current and hypothesized from compilations of long-termed moored current meter data (*Hogg*, 1983; *Hogg et al.*, 1986) is plausible, although the model resolution is comparable to the estimated meridional scale of the gyre. The recirculation gyre was estimated to carry 20–40 Sv (*Hogg*, 1983). This is larger than in the inversion (Figure 6a; Figure 9a), owing probably to the climatologic averaging and the coarse resolution.

In summary, a circulation scheme in the abyssal North Atlantic can be found that is consistent with (i) an estimate of density climatology, (ii) estimates of volume fluxes at specific locations (e.g., along the western boundary), and (iii) the constraints provided by a geostrophic finite-difference model. No severe contradiction is found between this circulation scheme and earlier estimates of the abyssal flow given the transport uncertainties. This circulation scheme is used below as a benchmark against which the effects of adding the information provided by ^{230}Th measurements are gauged.

5.2 Inversion of density and ^{230}Th data

5.2.1 Prior state and uncertainties

The state $\mathbf{x}$ is augmented to include the ^{230}Th activities at the model grid points. Likewise, the constraints $\mathbf{f}(\mathbf{x}) = \mathbf{0}$ and their uncertainty $\mathbf{C}_f$ are extended to include, respectively, the difference form (13) and its variance for each grid box (section 4.3.2). An objective mapping (Gauss–Markov smoother) is used to obtain an observational estimate of ^{230}Th and of its variance at each model grid point (these estimates are, respectively, in $\mathbf{x}_o$ and $\mathbf{C}_o$) from the ^{230}Th measurements and their errors at the data locations. Let $\mathbf{R}_{CC} = E(\mathbf{C}\mathbf{C}^{\mathrm{T}})$ be the second-moment matrix for ^{230}Th and $\mathbf{R}_{nn} = E(\mathbf{n}\mathbf{n}^{\mathrm{T}})$ the second-moment matrix for the ^{230}Th errors (noise). We assume

$$\{\mathbf{R}_{CC}\}_{ij} = r_0 \exp\left(-\frac{\Delta H(\mathbf{r}_i,\mathbf{r}_j)}{l_H}\right)\exp\left(-\frac{\Delta Z(\mathbf{r}_i,\mathbf{r}_j)}{l_Z}\right), \tag{14}$$

$$\{\mathbf{R}_{nn}\}_{ij} = r_{ij}\delta_{ij}. \tag{15}$$

Here $\Delta H(\mathbf{r}_i,\mathbf{r}_j)$ ($\Delta Z(\mathbf{r}_i,\mathbf{r}_j)$) is the horizontal (vertical) distance between the positions $\mathbf{r}_i$ and $\mathbf{r}_j$, l_H (l_Z) is a horizontal (vertical) correlation scale, r_0 is a variance estimate, r_{ii} is the ^{230}Th error at the ith data location, and δ_{ij} is the Kronecker delta ($\delta_{ij} = 1$ if $i = j$ and $\delta_{ij} = 0$ if $i \neq j$). Expression (14) states that the covariance between the ^{230}Th activities at two locations drops by e^{-1} if the horizontal (vertical) distance between the two locations increases by l_H (l_Z). Expression (15) states that the ^{230}Th errors are uncorrelated. Note that an estimate of the mean ^{230}Th in the deep North Atlantic is substracted from the ^{230}Th data prior to their use in objective mapping; this mean is then added to the objectively mapped values. The mean estimate is computed from

$$\tilde{m} = \left(\frac{1}{m_0^2} + \mathbf{d}^{\mathrm{T}}\mathbf{R}_{nn}^{-1}\mathbf{d}\right)^{-1}\mathbf{d}^{\mathrm{T}}\mathbf{R}_{nn}^{-1}\mathbf{y}, \tag{16}$$

where $m_0^2 = E(m^2)$, $\mathbf{d}^{\mathrm{T}} = (1, 1, \cdots, 1)$, and $\mathbf{y}$ is a vector including the ^{230}Th measurements. We assume $m_0 = 0.5$ dpm m^{-3}, which has no significant influence on the mean estimate ($m_0^{-2} \ll \mathbf{d}^{\mathrm{T}}\mathbf{R}_{nn}^{-1}\mathbf{d}$ in our case). Hence, we find $\tilde{m} = 0.44$ dpm m^{-3}.

The objective mapping of ^{230}Th data relies on three parameters: r_0, l_H, and l_Z. Consider first r_0. In the retained data set (235 values) 95% of the ^{230}Th measurements have an error ≤ 0.12 dpm m^{-3}. Here we assume $\sqrt{r_0} = 0.20$ dpm m^{-3}. Thus, far from data locations, the gridded ^{230}Th and its standard deviation approach, respectively, 0.44 dpm m^{-3} and 0.20 dpm m^{-3}. Consider then l_H and l_Z. In light of

the current uncertainties regarding the spatial covariance of ^{230}Th, two different cases will be considered. In a first case small correlation scales l_H and l_Z are assumed in mapping ^{230}Th. In a second case much larger values are used. Considering both cases is an attempt to explore how the uncertainties in the ^{230}Th distribution can influence inferences about the flow. Note that information about l_Z can be obtained from the ^{230}Th profiles with highest resolution (Figure 2). Each profile is first interpolated (not extrapolated) onto a regular grid with a vertical spacing equal to the mean sampling interval for that profile. Then the autocorrelation function of each interpolated profile is calculated. Only the first $n/4$ autocorrelation coefficients are considered, where n is the number of interpolated levels for a given profile. We find that the autocorrelation coefficients for each profile are all positive and decrease rapidly with increasing vertical spacing (Figure 10). The length scales characterizing the decreases are approximately in the range 200–1200 m. These values provide, respectively, a plausible lower and upper bound to l_Z.

In summary, for the inversions discussed below, the prior $\mathbf{x}_o$ should adjust to satisfy the linear vorticity balance, the density equation, and the radiochemical balance. The number of adjustable variables amounts to 4606 and the number of formal constraints is 3849. Although the level of formal underdeterminacy is higher than for the case where ^{230}Th is disregarded, it is expected that additional information about the flow will be obtained. As for the reference inversion, $\mathbf{C}_o$ and $\mathbf{C}_f$ are diagonal.

5.2.2 Case with small correlation scales

Here the objective mapping of ^{230}Th data assumes $l_H = 3 \times 10^5$ m ($\sim 3°$ of latitude, the resolution of the model) and $l_Z = 200$ m. To check the mapping we compare the mapped ^{230}Th at the data locations with the ^{230}Th measurements (not shown). The mapped and measured values are generally consistent given the uncertainties: only 2% of the mapped estimates differ by more than $2\sigma_{\mathrm{Th}}$ from the measurements. Given the small correlation scales, a large number of ^{230}Th activities and ^{230}Th activity errors at the model grid points approach the prior statistics $\tilde{m}$ and $\sqrt{r_0}$ (Figure 11). Thus, the present mapping can be regarded as a conservative estimate of the ^{230}Th distribution.

The gridded density and ^{230}Th values are inverted simultaneously. The cost function converges rapidly, being almost unchanged after 3 iterations (not shown). The prior estimates and formal constraints are generally satisfied (Figure 12). Interestingly, the residuals for the radiochemical balance are most generally negative (Figure 12b) – a result discussed below (section 6.1). The integrated meridional transports are

compared with those of the reference inversion (Figure 13a). The differences are not significant but systematic: the consideration of ^{230}Th data leads to a higher estimate of the transport amplitudes. They are dominated by differences in the depth-integrated flow at a small number of locations, i.e., a change in meridional transport is demanded by ^{230}Th data at some locations in the east but not in the west (Figure 14a). Note that the integrated transports at 22.5°N (-18.9 ± 3.1 Sv), 25.5°N (-18.8 ± 3.1 Sv), 34.5°N (-18.3 ± 3.1 Sv), and 37.5°N (-16.2 ± 3.1 Sv) are in the range of the estimates based on transatlantic sections at 25°N and 36°N (*Roemmich and Wunsch*, 1985; *Bryden et al.*, 2005).

To determine more conclusively the information brought by ^{230}Th we conduct another inversion where the standard deviation for the radiochemical balance (13) is reduced by 25% (0.075 Sv dpm m^{-3}), which is equivalent to increasing the weight for (13) by a factor $(0.1/0.075)^2 = 1.8$. The total cost converges after 3 iterations, and the posterior state is generally consistent with the prior state and the constraints (not shown). The higher confidence in (13) leads to the inference of an even larger amplitude of the integrated meridional transports below 1000 m, the differences with the values of the reference inversion being now greater than the posterior uncertainties (Figure 13b). The integrated transports at 22.5°N (-20.9 ± 3.0 Sv), 25.5°N (-20.8 ± 3.0 Sv), 34.5°N (-20.2 ± 3.0 Sv), and 37.5°N (-18.1 ± 3.0 Sv) are still compatible with the section estimates (*Roemmich and Wunsch*, 1985; *Bryden et al.*, 2005). In spite of the changes in the integrated transports, the flow structures of the reference inversion (Figures 6–9) persist when ^{230}Th data are considered in the analysis (assuming a standard deviation in (13) of 0.1 Sv dpm m^{-3} or 0.075 Sv dpm m^{-3}; not shown).

5.2.3 Case with large correlation scales

The ^{230}Th activities and their standard deviations at the model grid points are now estimated from more optimistic statistics in the objective mapping: $l_H = 3 \times 10^6$ m (comparable to the geographical extent of the basin) and $l_Z = 1200$ m (a plausible upper bound; Figure 10). The horizontal correlation scale is comparable to the scales assumed to map other water properties in the North Atlantic (e.g., *Fukomori and Wunsch* (1991)) and can hardly be rejected from the mapping diagnostics: only 4% of the mapped ^{230}Th at the data locations differ by more than $2\sigma_{\mathrm{Th}}$ from the ^{230}Th measurements (not shown). As expected, the gridded ^{230}Th display a stronger coherence on the basin scale (Figure 15a). At a depth of 3000 m, the ^{230}Th activity increases generally southward and eastward in the western part of the basin. In the eastern part, this pattern is interrupted by the occurrence of relatively low ^{230}Th at a couple of

stations near 25°N and 30°N (see also Figure 11a). The errors in the gridded ^{230}Th are smaller and have a more uniform distribution than in the case with low correlation scales (Figure 15b).

The second set of gridded ^{230}Th estimates is inverted simultaneously with density. The cost I converges after 3 iterations. The posterior state fulfills generally the prior state and the constraints (e.g., 20 over 23 of the integrated flux constraints along the western boundary are satisfied). The integrated meridional transports differ from the ones estimated without the ^{230}Th data by more than one standard deviation (Figure 16a), the differences being larger if the radiochemical balance is deemed more accurate (Figure 16b). These differences arise from a change in the meridional component of transport that is distributed more equally throughout the basin than for the case with small ^{230}Th correlation scales (compare Figure 14a with Figure 14b). If a standard deviation of 0.1 Sv dpm m^{-3} is assumed for (13), the integrated transports at 22.5°N (-22.5 ± 2.8 Sv), 25.5°N (-22.4 ± 2.8 Sv), 34.5°N (-21.9 ± 2.8 Sv), and 37.5°N (-19.9 ± 2.8 Sv) remain compatible with the estimates based on transatlantic sections (*Roemmich and Wunsch*, 1985; *Bryden et al.*, 2005). If a deviation of 0.075 Sv dpm m^{-3} is assumed, the integrated transports at these latitudes (from -25.9 ± 2.6 Sv to -23.3 ± 2.6 Sv) all exceed these estimates by more than one standard deviation. Besides, flow structures in the interior are more coherent compared to those of the reference inversion. A notable feature is the broad southward flow between 2000 and 3000 m that is demanded by the ^{230}Th data; this flow is particularly apparent if a standard deviation of 0.075 Sv dpm m^{-3} is assumed for (13) (Figure 17a). The uncertainties in the individual transports estimated a posteriori are reduced (compare Figure 7b with Figure 17b), although this is not very apparent from our convention of plotting the errors in these figures (see below section 6.2).

6 Discussion

The different circulation estimates in the deep North Atlantic obtained in this work show that the consideration of ^{230}Th data leads to the inference of a larger amplitude of the integrated meridional transports (compared to a circulation estimated only from more conventional information provided by a hydrographic climatology and volume fluxes at specific locations). In this section, we examine this result in more detail and discuss the increased determinacy of the flow resulting from the incorporation of ^{230}Th.

6.1 Inference of larger meridional transports

The dynamical balances (8–12) used to constrain the flow have the state of rest as a possible solution, unless the horizontal density gradients do not vanish. Such gradients, however, are very small in the abyssal interior. Thus, circulation schemes constrained by (8–12) have a tendency towards small transport amplitudes. The consideration in the flow estimation of the available ^{230}Th data leads to the inference of a more vigorous circulation, owing to the additional requirement that the divergence of the tracer flux must balance the tracer source within uncertainty estimates. This interpretation is supported by the fact that most residuals for the radiochemical balance (13) have the same sign (Figure 12b). That is, in order to comply with both the dynamics (8–12) and (13), the inversion leads to a solution that is heavily skewed towards the inability of $\nabla \cdot (\mathbf{u}_e C)$ to balance J_p. This bias persists if a much larger value $w_* = 200$ m yr^{-1} – probably an unrealistic assumption – is used (inversion with low correlation scales for ^{230}Th mapping; not shown), suggesting that it is an intrinsic feature.

Note that a bias in equation residuals has been found in earlier studies based on inverse circulation models. In their study of the North Atlantic, *Mercier et al.* (1993) showed that most residuals in the vertically integrated form of the heat equation are negative (their Fig. 22). These residuals provide information about the heat flux at the surface that is not represented explicitly in the equation. The apparent skewness of these residuals would then reflect, at least partly, the tendency for the investigated oceanic area to gain or receive heat through the surface.

We make three comments regarding the correction by ^{230}Th for the tendency of a no flow solution. First, a state of rest may not be a solution of (8–12) if some of the terms neglected in these equations are given an explicit form. For example, if mixing terms are represented as Fickian diffusion in (12), a state of rest would not be a solution, although a sluggish circulation may again result if the second-order derivatives of the density field are not significant. Here the effects of mixing are represented implicitly (i.e., in the equation residuals), as in earlier studies (e.g., *Wunsch and Grant* (1982); *Mercier* (1989); *Vanicek and Siedler* (2002)). Second, even if horizontal density gradients are not significant, the inferred flow may not be a state of rest if density errors along the same geopotential surface show a positive covariance: in this case an error at one location coexists with an error of the same sign at another location along the same surface, thereby maintaining a non-zero baroclinic production of vorticity. Thus, a nondiagonal $\mathbf{C}_o$ may prevent a no flow solution in situations where the density field is relatively noisy. Finally, the relative

effects of ^{230}Th in the flow inference may depend on the assumed accuracy of the dynamical constraints: a higher accuracy may imply a better capability of the density field to provide information about the flow and perhaps a reduced capability of ^{230}Th to complement density. To examine this possibility we perform two additional inversions where the standard deviations for (9–12) are reduced by half compared to the reference inversion. One inversion is contrained by ^{230}Th (with small correlation scales for objective mapping), whereas the other is not. As for the previous comparison (Figure 13a), we find insignificant but systematic differences in the integrated meridional transports between the two inversions: the transport amplitudes are larger by 2 Sv if ^{230}Th is considered. Thus, the inference of larger transport amplitudes to accomodate the information provided by ^{230}Th seems robust against the uncertainties assumed for the dynamics.

6.2 Increased determinacy of the flow

An interesting question is, to what extent can the information brought by ^{230}Th reduce the uncertainties in the estimate of the abyssal circulation? Consider first the case with small correlation scales for ^{230}Th mapping. The integrated meridional transports vary with latitude from -19.1 ± 3.1 Sv to -15.9 ± 3.1 Sv if the standard deviation for the radiochemical balance (13) is fixed at 0.1 Sv dpm m^{-3}. They range from -21.1 ± 3.0 Sv to -17.7 ± 2.9 Sv if this deviation is reduced to 0.075 Sv dpm m^{-3}. Thus, the addition of ^{230}Th leads to only a modest gain in the absolute and relative precisions of the integrated transports (in the reference inversion the integrated transports range from -16.8 ± 3.4 Sv to -13.9 ± 3.4 Sv). We then compare the errors in the individual horizontal transports. In the reference inversion, only 47% of the transports have an error $\leq$ 1.5 Sv (short dashed line in Figure 18a). This percentage rises to 60% and 65% if ^{230}Th is incorporated in the analysis (respectively, long dashed and solid lines in Figure 18a), the largest rise occurring for the largest confidence in (13). Thus, conservative assumptions about the ^{230}Th distribution lead to only a marginal increase in the determinacy of the abyssal flow.

Consider now the case with large correlation scales for ^{230}Th mapping. In this case, the integrated meridional transports range from -22.6 ± 2.8 Sv to -19.5 ± 2.8 Sv if a standard deviation of 0.1 Sv dpm m^{-3} is used for (13). They range from -26.1 ± 2.6 Sv to -22.8 ± 2.6 Sv if this deviation is fixed at 0.075 Sv dpm m^{-3}. For the smallest deviation, the absolute and relative errors are reduced by, respectively, 0.8 Sv and a factor of two compared to the reference inversion. The fraction of individual horizontal

transports that have an error $\leq$ 1.5 Sv rises to 66% for a deviation of 0.1 Sv dpm m^{-3} and to 70% for a deviation of 0.075 Sv dpm m^{-3} (Figure 18b). As expected, more optimistic assumptions about the ^{230}Th distribution imply a better determinacy of the flow.

7 Conclusions and Perspectives

An inverse finite-difference model of the abyssal circulation in the North Atlantic basin has been developed in order to evaluate the dynamical information contained in measurements of ^{230}Th. We have attempted to rely on all existing ^{230}Th data, used a dynamically consistent model, and considered explicitly the uncertainties in the various observational and formal constraints of the method. Comparing different circulation estimates allowed us to quantify the amount of information brought by the addition of ^{230}Th data in the inference of the time mean flow. We found that the addition of these data leads to (i) a larger amplitude of the integrated meridional transports; and (ii) a marginal increase in the determinacy of the flow. Result (i) is interpreted in terms of a tendency of geostrophic dynamics to lead to the inference of a vanishing circulation when horizontal density gradients are not significant. This tendency is counteracted by the ^{230}Th activity data, which show large differences in the abyssal interior, and the attendant constraint that the divergence of the tracer flux must balance the tracer source.

We discuss some limitations of this work so as to identify possible perspectives. First, needless to say, the present investigation will need to be extended by a more extensive ^{230}Th data base (*Anderson and Henderson*, 2005). There are important gaps in the distribution of ^{230}Th in the North Atlantic, even though this is the basin where most ^{230}Th measurements are available. Our working hypotheses that ^{230}Th measurements originating from different laboratories are internally compatible and that they can, by and large, be treated as synoptic should be examined. For example, *Moran et al.* (2002) observed an increase in ^{230}Th activity in the Labrador Sea from 1993 to 1999, which was ascribed to a cessation of local deep convection since 1993. Whether similar changes can occur elsewhere in the North Atlantic will need to be investigated. Second, the present work relies on the hypothesis that the possible spatial variations in ^{230}Th scavenging can be represented implicitly. Two arguments indicate that these variations do not dominate the spatial variations in ^{230}Th activity observed in the North Atlantic. A large number of ^{230}Th profiles from distant locations exhibit the same trend in the upper 1000 m and diverge below (e.g., Figure 2). If variations in scavenging intensity were responsible for the activity variations, one

would expect to observe activity differences throughout the water column – not only in deep water – as many particles are produced through biological activity near the surface (this argument, however, fails if for some reason spatial variations in scavenging occur only deeper than 1000 m). Moreover, the ^{230}Th mapping estimated from large correlation scales reveals a distribution that is consistent with intuition regarding the effect of the circulation on the tracer, with low activity values near the northern and western boundaries and higher values in the eastern interior (Figure 15a). Here an effort has been made to express ^{230}Th scavenging in terms of two parameters that can be determined in situ – at least in principle: w_s and K. The present analysis could easily be extended by the provision of more accurate information about both parameters in the abyssal North Atlantic (see *Henderson et al.* (1999) for an attempt to account for spatial variations in ^{230}Th partitioning in a global three-dimensional forward model).

Acknowledgements.

We thank Ruth Curry for sharing with us the data from *HydroBase*. Comments by two anonymous reviewers and the editor significantly improved the manuscript. Peter Huybers, Jerry McManus, and Carl Wunsch provide detailed and useful comments. We are indebted to Charles Jackson and members of the Texas Advanced Computer Center of the University of Texas at Austin for giving access to their facilities. OM acknowledges the support from the Ocean and Climate Change Institute at WHOI and from the U.S. National Science Foundation. The IAEA (JS) is grateful for the support provided to its Marine Environment Laboratory by the Government of the Principality of Monaco. JS is grateful to Jan Fietzke for ICPMS measurements and for support from the 'Deutsche Forschungsgemeinschaft' (grant no. SCHO752/ 2-1). This work is dedicated to the late Prof. Roland Wollast, who introduced two of the authors (OM and RF) to chemical oceanography and provided them with a model of scientific excellence.

Appendix

François and co-workers measured seawater ^{230}Th concentration using an ICP-MS (Finnigan MAT Element), as described in *Choi et al.* (2001). Briefly, 15–20 L water samples obtained by hydrocasts using Niskin bottles were immediately drained (for total ^{230}Th) or filtered through 0.8 mm pore size Versapor filters (for dissolved ^{230}Th) into 20 L polyethylene collapsible cubitainers. Samples were weighed with a precision better than 1% on a computerized balance that averages out the acceleration from the ship's motion. They were acidified with 30 ml 6N HCl and spiked with ^{229}Th and 1 ml $FeCl_3$ (50 mg ml^{-1}). After $\sim$ 12 hours equilibration, the pH was adjusted to $\sim$ 8.5–9 with NH_4OH to precipitate Fe oxyhydroxides

that adsorb dissolved and entrain particulate Th. This was followed by decantation, centrifugation, and storage for analysis. The analytical procedure included a purification step by anion-exchange using AG1-X8 resin and isotope ratio ($^{230}Th/^{229}Th$) measurements using a desolvating micronebulizer for sample introduction into the plasma of the mass spectrometer. Internal precision was $\sim 2\%$ and reproducibility $\sim 5\%$ (95% confidence interval) in deep water.

Scholten and co-workers obtained water samples using Niskin bottles mounted on a CTD. For the determination of total (particulate and dissolved) Th isotopes, 1–2 litre of water were filled in pre-cleaned polyethylene containers. The samples were weighed, spiked with ^{229}Th, and acidified with suprapure HNO_3. After 24 hours NH_4OH was added so that $MgOH_2$ precipitated. The precipitate was allowed to settle and after decanting the precipitate was transferred into 250 ml polyethylene bottles. In order to reduce the amount of precipitate 7N HNO_3 was carefully added to the Th water sample to reduce the amount of precipitate. Samples had to be shaken after each acid addition. The resulting precipitate was transferred into 50 ml centrifuge tubes and further reduced by nitric acid addition. Samples were centrifuged, decanted, and dissolved in 25 ml of 7N HNO_3. The main goal of the anion exchange column separation is the removal of Mg. Therefore BioRad 10 ml polypropylene columns were loaded with 2 ml BioRad AG 1×8 resin. The resin and column were cleaned twice (20 ml 7N HNO_3, 20 ml 7N HCl, 20 ml H_2O) and preconditioned (20 ml 7N HNO_3). The dissolved sample was put onto the column. Mg passed through the column and was completely removed with 20 ml 7N HNO_3. Thorium was eluted with 10 ml 7N HCl into a Teflon beaker, and 50 μl of $HCLO_4$ added to decompose any residual resin. The solution was evaporated to dryness. After addition of 3 ml 5% HNO_3 the samples were ready for the ICP-MS analysis. All sample preparations were carried out in a clean lab environment. Ultra pure water (18.2 MOhm), suprapure $HClO_4$, subboiled distilled HCl, HF, and HNO_3 were used for all chemical treatments. The measurements were performed on a Micromass Plasma Trace 2, a double focussing ICP-MS with reverse Nier-Johnson geometry. Desolvation was achieved with a Cetac MCN-6000. A self aspiring microconcentric glass nebulizer ("MicroMist" 100 μl) with 120 μl min^{-1} sample uptake rate introduces the aerosol into a heated PFA spray chamber. The aerosol is desolvated by a heated membrane and introduced into the plasma. For a more effective cone cooling, Ni cones with a Cu core (Chilton RAC705 and RAC19) were used. The nebulizer and the spraychamber of the Cetac MCN6000 were cleaned after each measurement using 5% HNO3. Measurements of Th isotopes were carried out in 400Res mass resolution modes to ensure maximum sensitivity. For seawater samples (with relatively high $^{230}Th/^{232}Th$ mass ratio

of approximately 4–10), abundance sensitivity is not critical. ^{229}Th, ^{230}Th, and ^{232}Th were measured in one scan. Each scan contained 4 points in the centre of the flat top region (centre ± 0.03 amu) of each peak. Integration time for one point was 1 s for ^{229}Th and ^{232}Th and 4 s for ^{230}Th. About 50 scans were recorded for one measurement. Thus resulting acquisition time for one sample was about 25 min. All measured ^{230}Th concentrations were corrected for detrital, U-supported ^{230}Th concentrations to obtain excess activities $^{230}\mathrm{Th}_{ex} = {}^{230}\mathrm{Th} - 0.7\times{}^{232}\mathrm{Th}$, where ^{230}Th and ^{232}Th are the measured activities and 0.7±0.2 is the average $^{238}\mathrm{U}/^{232}\mathrm{Th}$ ratio.

References

Anderson, R. F., M. P. Bacon, and P. G. Brewer, Removal of ^{230}Th and ^{231}Pa at ocean margins, *Earth Planet. Sci. Lett.*, *66*, 73–90, 1983a.

Anderson, R. F., M. P. Bacon, and P. G. Brewer, Removal of ^{230}Th and ^{231}Pa from the open ocean, *Earth Planet. Sci. Lett.*, *62*, 7–23, 1983b.

Anderson, R. F., M. Q. Fleisher, P. E. Biscaye, N. Kumar, B. Dittrich, P. Kubik, and M. Suter, Anomalous boundary scavenging in the Middle Atlantic Bight: Evidence from ^{230}Th, ^{231}Pa, ^{10}Be and ^{210}Pb, *Deep-Sea Res. II*, *41*, 537–561, 1994.

Anderson, R. F., and G. M. Henderson, GEOTRACES: A global study of the marine biogeochemical cycles of trace elements and their isotopes, *Oceanography*, *18*, 76–79, 2005.

Bacon, M. P., Tracers of chemical scavenging in the ocean: Boundary effects and large scale chemical fractionation, *Phil. Trans. Roy. Soc., London*, *320*, 187–200, 1988.

Bacon, M. P., and R. F. Anderson, Distribution of thorium isotopes between dissolved and particulate forms in the deep sea, *J. Geophys. Res.*, *87*, 2045–2056, 1982.

Bacon, M. P., and M. M. Rutgers van der Loeff, Removal of thorium-234 by scavenging in the bottom nepheloid layer of the ocean, *Earth Planet. Sci. Lett.*, *92*, 157–164, 1989.

Baringer, M., and J. Price, Mixing and spreading of the Mediterranean Outflow, *J. Phys. Oceanogr.*, *27*, 1654–1677, 1997.

Bretherton, F. P., R. E. Davis, and C. B. Fandry, A technique for objective analysis and design of oceanographic experiments applied to MODE-73, *Deep-Sea Res.*, *23*, 559–582, 1976.

Broecker, W. S., and T.-H. Peng. *Tracers in the Sea.* Lamont-Doherty Geological Observatory, Palisades, NY: Eldigio Press, 1982.

Bryden, H. L., H. R. Longworth, and S. A. Cuningham, Slowing of the Atlantic meridional overturning circulation at 25°N, *Nature*, *doi:10.1038/nature04385*, 655–657, 2005.

Chase, Z., R. F. Anderson, M. Q. Fleisher, and P. W. Kubik, The influence of particle composition and particle flux on the scavenging of Th, Pa and Be in the ocean, *Earth Planet. Sci. Lett.*, *204*, 215–229, 2002.

Cheng, H., R. L. Edwards, J. Hoff, C. D. Gallup, D. A. Richards, and Y. Asmerom, The half-lives of uranium-234 and thorium-230, *Chem. Geol.*, *169*, 17–33, 2000.

Choi, M.-S., R. François, K. Sims, M. P. Bacon, S. Brown-Leger, A. P. Fleer, L. Ball, D. Schneider, and S. Pichat, Rapid determination of ^{230}Th and ^{231}Pa in seawater by desolvated-micronebulization Inductively-Coupled Magnetic Sector Mass Spectrometry, *Mar. Chem.*, *76*, 99–112, 2001.

Cochran, J. K., H. D. Livingston, D. J. Hirschberg, and L. D. Surprenant, Natural and anthropogenic radionuclide distributions in the northwestern Atlantic Ocean, *Earth Planet. Sci. Lett.*, *84*, 135–152, 1987.

Colley, S., J. Thomson, and P. P. Newton, Detailed ^{230}Th, ^{232}Th, and ^{210}Pb fluxes recorded by the 1989/90 BOFS sediment trap time-series at 48°N, 20°W, *Deep-Sea Res. I*, *42*, 833–848, 1995.

Curry, R., 2001. Hydrobase 2 - A database of hydrographic profiles and tools for climatological analysis. Woods Hole Oceanographic Institution, Technical reference, preliminary draft, Woods Hole, USA.

Fine, R. A., and R. L. Molinari, A continuous deep western boundary current between Abaco (26.5°N) and Barbados (13°N), *Deep-Sea Res.*, *35*, 1441–1450, 1988.

Fukomori, I., and C. Wunsch, Efficient representation of the North Atlantic hydrographic and chemical distributions, *Prog. Oceanogr.*, *27*, 111–195, 1991.

Gill, A. E. *Atmosphere-Ocean Dynamics*, Volume 30 of *Int. Geophys. Ser.* Academic, San Diego, Calif., 1982. 662 pp.

Guo, L., M. Chen, and C. Gueguen, Control of Pa/Th ratio by particulate chemical composition in the ocean, *Geophys. Res. Let.*, *29*, doi:10.1029/2002GL015666, 2002.

Henderson, G. M., C. Heinze, R. F. Anderson, and A. M. E. Winguth, Global distribution of the ^{230}Th flux to ocean sediments constrained by GCM modelling, *Deep-Sea Res. I*, *46*, 1861–1893, 1999.

Hogg, N., and W. B. Owens, Direct measurement of the deep circulation within the Brazil Basin, *Deep-Sea Res. I*, *46*, 335–353, 1999.

Hogg, N. G., A note on the deep circulation of the western North Atlantic: Its nature and causes, *Deep-Sea Res.*, *30*, 945–961, 1983.

Hogg, N. G., R. S. Pickart, R. M. Hendry, and W. J. Smethie, The Northern Recirculation Gyre of the Gulf Stream, *Deep-Sea Res.*, *33*, 1139–1165, 1986.

Krishnaswami, S., D. Lal, B. L. K. Somayajulu, R. F. Weiss, and H. Craig, Larve volume in-situ filtration of deep Pacific waters: Mineralogical and radioisotope studies, *Earth Planet. Sci. Lett.*, *32*, 420–429, 1976.

Krishnaswami, S., M. M. Sarin, and B. L. K. Somayajulu, Chemical and radiochemical investigations of surface and deep particles of the Indian Ocean, *Earth Planet. Sci. Lett.*, *54*, 81–96, 1981.

Lozier, M. S., W. B. Owens, and R. G. Curry, The climatology of the North Atlantic, *Prog. Oceanogr.*, *36*, 1–44, 1995.

Mangini, A., and R. M. Key, A ^{230}Th profile in the Atlantic Ocean, *Earth Planet. Sci. Lett.*, *62*, 377–384, 1983.

Martel, F., and C. Wunsch, The North Atlantic circulation in the early 1980s - An estimate from inversion of a finite-difference model, *J. Phys. Oceanogr.*, *23*, 898–924, 1993.

Mercier, H., Determining the general circulation of the ocean: A nonlinear inverse problem, *J. Geophys. Res.*, *91*, 5103–5109, 1986.

Mercier, H., A study of the time-averaged circulation in the western North Atlantic by simultaneous nonlinear inversion of hydrographic and current meter data, *Deep-Sea Res.*, *36*, 297–313, 1989.

Mercier, H., M. Ollitraut, and P. Y. Le Traon, An inverse model of the North Atlantic general circulation using Lagrangian float data, *J. Phys. Oceanogr.*, *23*, 689–715, 1993.

Molinari, R. L., R. A. Fine, and E. Johns, The Deep Western Boundary Current in the tropical North Atlantic Ocean, *Deep-Sea Res.*, *39*, 1967–1984, 1992.

Moran, S. B., M. A. Charette, J. A. Hoff, R. L. Edwards, and W. M. Landing, Distribution of ^{230}Th in the Labrador Sea and its relation to ventilation, *Earth Planet. Sci. Lett.*, *150*, 151–160, 1997.

Moran, S. B., C.-C. Shen, H. N. Edmonds, S. E. Weinstein, J. N. Smith, and R. L. Edwards, Dissolved and particulate ^{231}Pa and ^{230}Th in the Atlantic Ocean: Constraints on intermediate/deep water age, boundary scavenging, and ^{231}Pa/^{230}T fractionation, *Earth Planet. Sci. Lett.*, *203*, 999–1014, 2002.

Morris, M. Y., M. M. Hall, S. L. C., and N. G. Hogg, Abyssal mixing in the Brazil Basin, *J. Phys. Oceanogr.*, *31*, 3331–3348, 2001.

Nozaki, Y., Y. Horibe, and H. Tsubota, The water column distributions of thorium isotopes in the western North Pacific, *Earth Planet. Sci. Lett.*, *54*, 203–216, 1981.

Ochoa, J., and N. A. Bray, Water mass exchange in the Gulf of Cadiz, *Deep-Sea Res.*, *38*, 465–503, 1991.

Olbers, D. J., M. Wenzel, and J. Willebrand, The inference of North Atlantic circulation patterns from climatological hydrographic data, *Rev. Geophys.*, *23*, 313–356, 1985.

Pickart, R. S., Water mass components of the North Atlantic deep western boundary current, *Deep-Sea Res.*, *39*, 1553–1572, 1992.

Robinson, L. F., N. S. Belshaw, and G. M. Henderson, U and Th concentrations and isotope ratios in modern carbonates and waters from the Bahamas Bank, *Geochim. Cosmochim. Acta*, *68*, 1777–1789, 2004.

Roemmich, D., and C. Wunsch, Two transatlantic sections: Meridional circulation and heat flux in the subtropical North Atlantic Ocean, *Deep-Sea Res.*, *32*, 619–664, 1985.

Roy-Barman, M., J. H. Chen, and G. J. Wasserburg, ^{230}Th–^{232}Th systematics in the central Pacific Ocean: The sources and fates of thorium, *Earth Planet. Sci. Lett.*, *139*, 351–363, 1996.

Roy-Barman, M., C. Jeandel, M. Souhaut, M. Rutgers van der Loeff, I. Voege, N. LeBlond, and R. Freydier, The influence of particle composition on thorium scavenging in the NE Atlantic ocean (POMME experiment), *Earth Planet. Sci. Lett.*, *240*, 681–693, 2005.

Rutgers van der Loeff, M. M., and G. W. Berger, Scavenging of ^{230}Th and ^{231}Pa near the Antarctic Polar Front in the South Atlantic, *Deep-Sea Res. I*, *40*, 339–357, 1993.

Santschi, P. H., J. W. Murray, M. Baskaran, C. R. Benitez-Nelson, L. D. Guo, C.-C. Hung, C. Lamborg, S. B. Moran, U. Passow, and M. Roy-Barman, Thorium speciation in seawater, *Mar. Chem.*, *100*, 250–268, 2006.

Schmitz, W. J., 1996. On the World Ocean Circulation - Some Global Features - North Atlantic Circulation. Woods Hole Oceanographic Institution - Technical Report WHOI-96-03.

Schmitz, W. J., and M. S. McCartney, On the North Atlantic circulation, *Rev. Geophys.*, *31*, 29–49, 1993.

Scholten, J. C., J. Fietzke, S. Vogler, M. M. Rutgers van der Loeff, A. Mangini, W. Koeve, J. Waniek, P. Stoffers, A. Antia, and J. Kuss, Trapping efficiencies of sediment traps from the deep Eastern North Atlantic: The ^{230}Th calibration, *Deep-Sea Res. I*, *48*, 2383–2408, 2001.

Scholten, J. C., M. M. Rutgers van der Loeff, and A. Michel, Distribution of ^{230}Th and ^{231}Pa in the water column in relation to the ventilation of the deep Arctic basins, *Deep-Sea Res. I*, *42*, 1519–1531, 1995.

Stephens, J. C., and D. P. Marshall, Dynamical pathways of Antarctic Bottom Water in the Atlantic, *J. Phys. Oceanogr.*, *30*, 622–640, 2000.

Talley, L. D., Shallow, intermediate, and deep overturning components of the global heat budgets, *J. Phys. Oceanogr.*, *33*, 530–560, 2003.

Tarantola, A., and B. Valette, Generalized nonlinear inverse problem solved using the least squares criterion, *Rev. Geophys. Space Phys.*, *20*, 219–232, 1982.

Vanicek, M., and G. Siedler, Zonal fluxes in the deep water layers of the western south Atlantic Ocean, *J. Phys. Oceanogr.*, *32*, 2205–2235, 2002.

Vogler, S., J. Scholten, M. Rutgers van der Loeff, and A. Mangini, ^{230}Th in the eastern North Atlantic: the importance of water mass ventilation in the balance of ^{230}Th, *Earth Planet. Sci. Lett.*, *156*, 61–74, 1998.

Wunsch, C., The North Atlantic general circulation west of 50°W determined by inverse methods, *Rev. Geophys. Space Phys.*, *16*, 583–620, 1978.

Wunsch, C. *Discrete inverse and state estimation problems.* Cambridge University Press, 2006. 371 pp.

Wunsch, C., and B. Grant, Towards the general circulation of the North Atlantic Ocean, *Prog. Oceanogr.*, *11*, 1–59, 1982.

Yu, E.-F., R. François, and M. P. Bacon, Similar rates of modern and last-glacial ocean thermohaline circulation inferred from radiochemical data, *Nature*, *379*, 689–694, 1996.

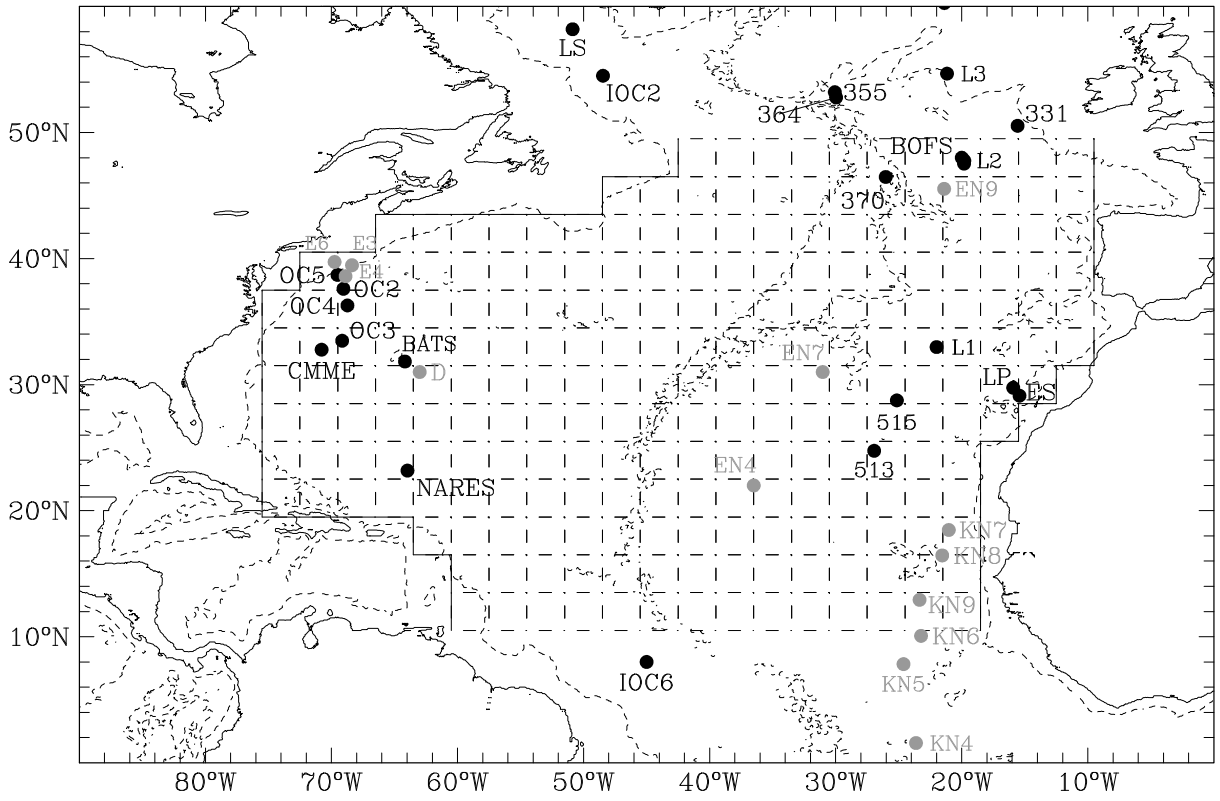

Figure 1: Distribution of stations in the North Atlantic where measurements of ^{230}Th activity in the water column are available (for the original references see Table 1). The geographic locations of the new ^{230}Th measurements (section 2.2) can be identified from this Table (cf. 'unpub.'). Black dots show stations where measurements of both dissolved and particulate ^{230}Th or measurements of total ^{230}Th are available. Grey dots show stations where only measurements of dissolved ^{230}Th are available. The isobaths of 0 m (solid line) and 3000 m (dashed line) and the model grid (latitude and longitude lines) are also displayed.

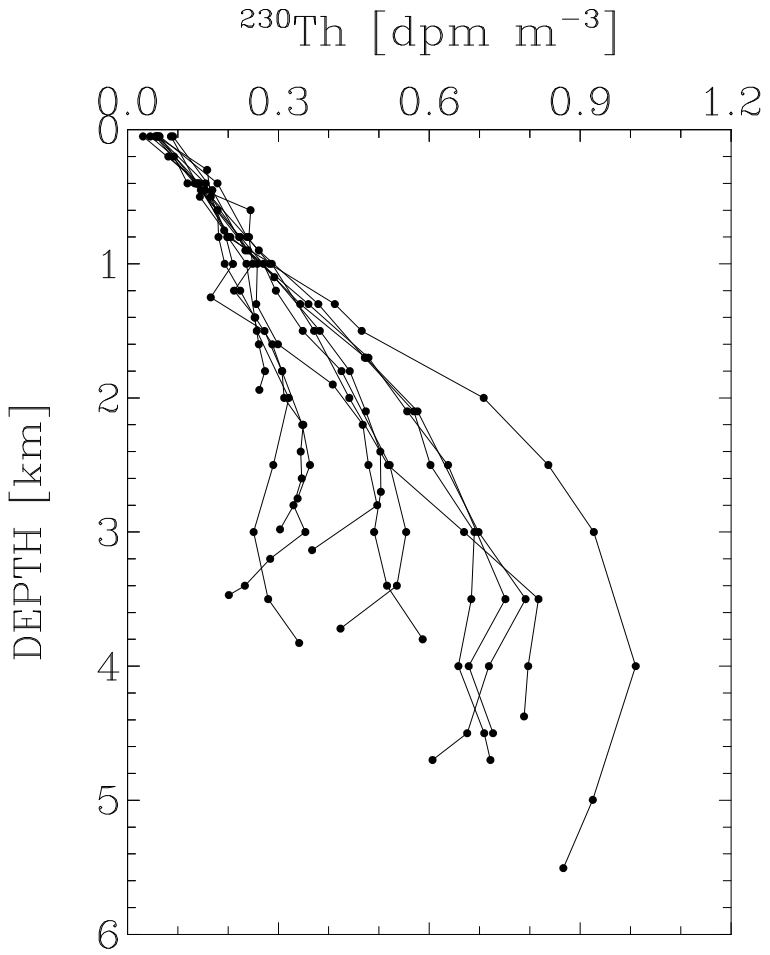

Figure 2: Vertical distribution of dissolved ^{230}Th at 12 stations in the North Atlantic: stations E3, E4, and E6, stations EN4, EN7, EN9, and stations KN4–9 (Table 1; Figure 1). The errors in the ^{230}Th measurements are not shown (unpublished data from R. François).

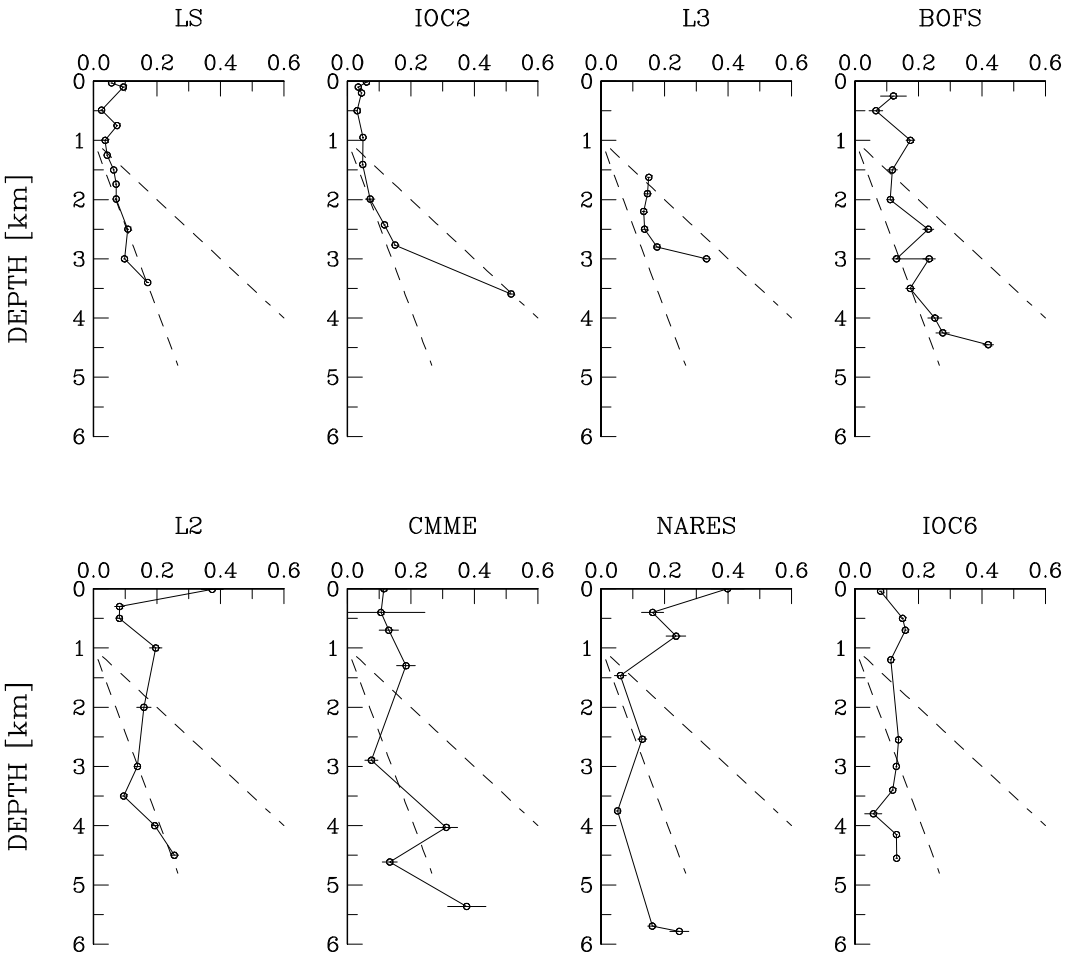

Figure 3: Vertical distribution of the partition coefficient K (circles) at eight stations in the North Atlantic where measurements of both dissolved and particulate ^{230}Th are available. The horizontal bars are one standard deviation computed from the reported errors in the measurements of dissolved and particulate ^{230}Th assuming that these errors are uncorrelated. The K maxima at stations IOC2 (at z = 3593 m), L3 (3000 m), and BOFS (4450 m) may result from the proximity of the seafloor (respectively, at z = 3713, 3050, and 4540 m). The two dashed lines show the vertical gradient $\partial K/\partial z$ required for the term $w_s C \partial K/\partial z$ to be comparable to the production term J_p, computed for the case where w_s = 300 m yr^{-1} and 900 m yr^{-1}. For both lines, we assume $J_p = 2.7 \times 10^{-2}$ dpm m^{-3} yr^{-1} and $C = 0.44$ dpm m^{-3} (see text for details and Table 1 for data references).

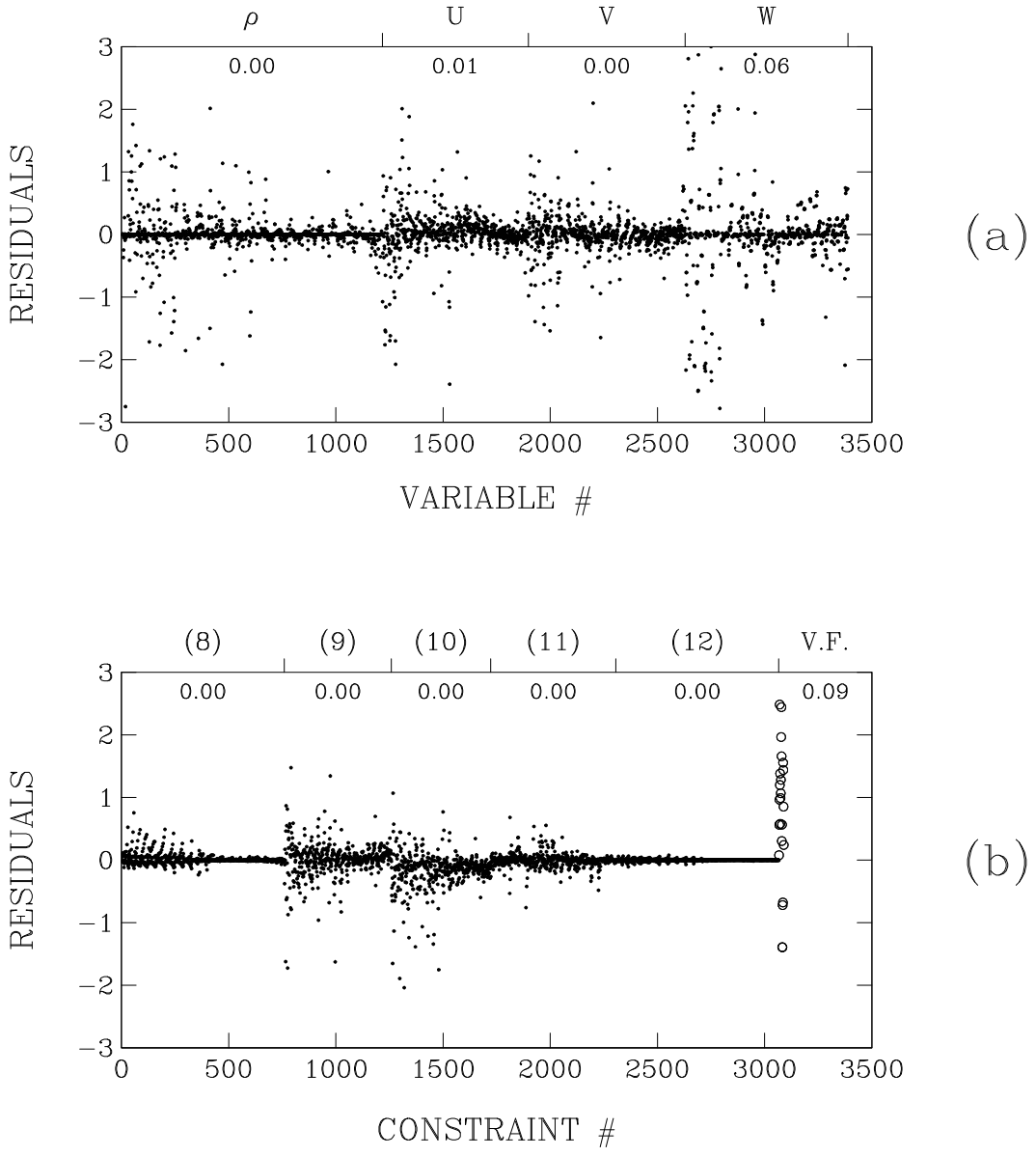

Figure 4: Diagnostics of the inversion of density data. (a) Normalized residuals for density (ρ) and the three transport components (U, V, W). (b) Normalized residuals for the dynamical balances (8–12) (solid circles) and the volume transports along the western boundary (V.F.; open circles). For each panel, the values below the top horizontal axis are the fractions of normalized residuals that are ≥ 2 in absolute magnitude.

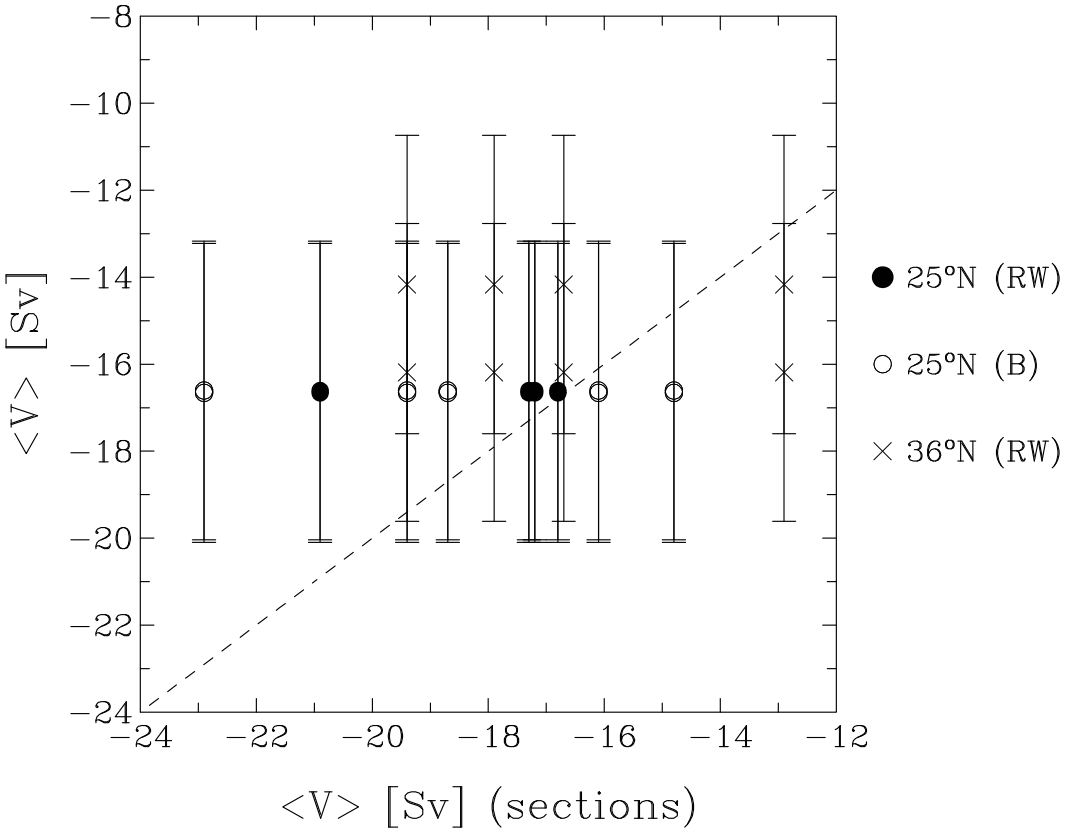

Figure 5: Comparison between the integrated meridional transports inferred in this study (vertical axis) and estimated from transatlantic sections (horizontal axis). The observational estimates are from (i) *Roemmich and Wunsch* (1985) (RW), based on sections at 25°N (more exactly, 24.5°N) and 36°N (36.25°N), and from (ii) *Bryden et al.* (2005) (B), based on sections at 25°N (24.5°N). They are compared to the integrated transports inferred here at the encompassing latitudes: 22.5°N and 25.5°N for the section at 24.5°N and 34.5°N and 37.5°N for the section at 36.25°N. The vertical bars are the standard deviations in the posterior transports. The dashed line is the line of perfect agreement.

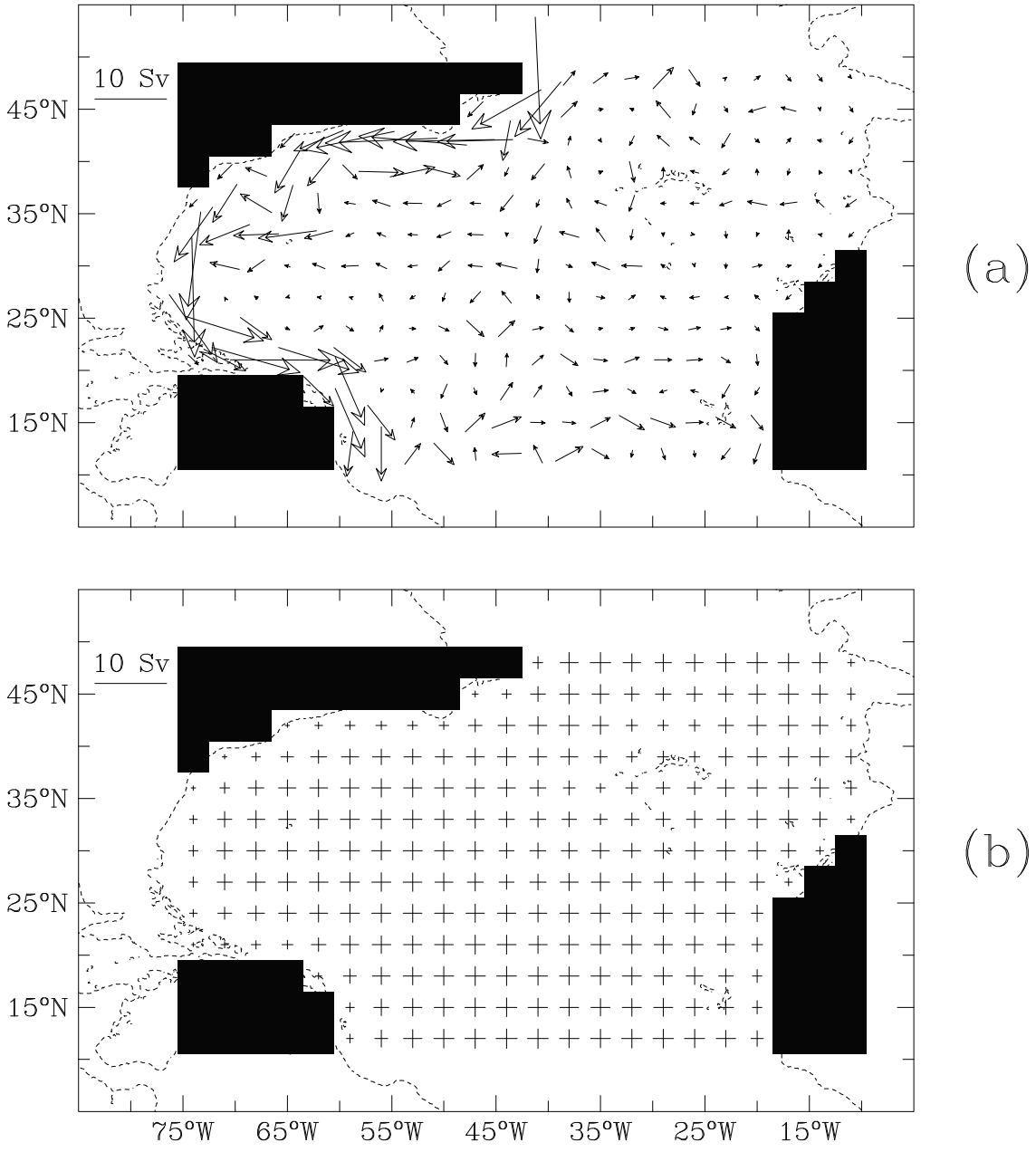

Figure 6: Distribution of (a) the horizontal transport integrated between 1000 and 4000 m and (b) its error as estimated from the reference inversion. In panel (a) the vectors, which occur at the center of the model grid boxes, have been computed by averaging the zonal and meridional components of transport defined at the box faces. In panel (b) the horizontal (vertical) lines show the standard deviations for the zonal (meridional) components of the integrated transport. The relatively small deviations along the lateral boundaries are largely due to our assumption that these boundaries are perfectly rigid, i.e., the standard deviation for the transport component normal to these boundaries is zero. In both panels, the black areas and the dashed line show, respectively, the model topography and the 1000 m isobath.

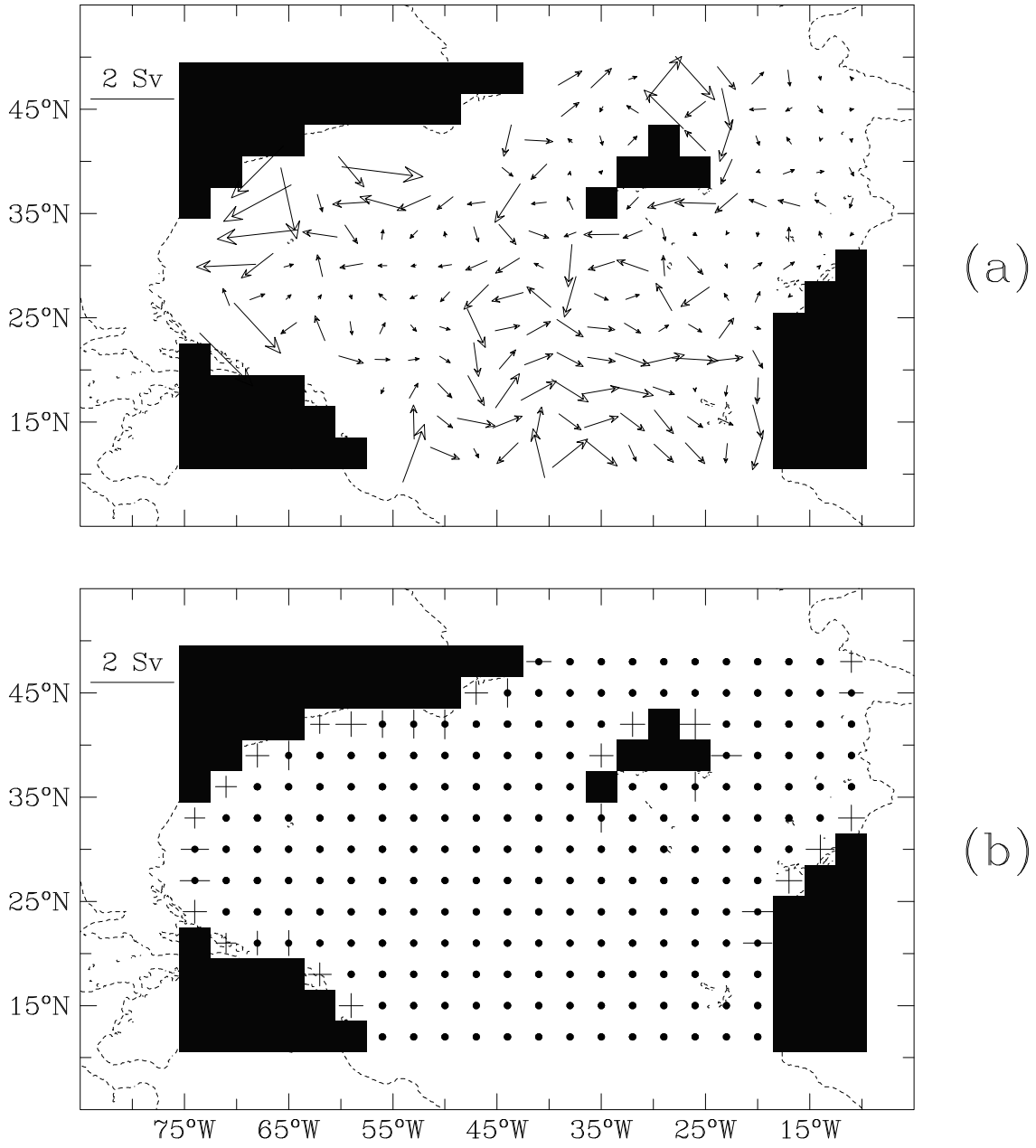

Figure 7: Distribution of (a) the horizontal transport in the layer between 2000 and 3000 m and (b) its error as estimated from the reference inversion. In panel (a) the transports with an amplitude > 2 Sv are omitted to avoid congestion of the figure. In panel (b) the horizontal (vertical) lines show the standard deviations for the zonal (meridional) components of the transport. The presence of a black dot signifies that the error in at least one component has a scale larger that the grid size (3°). The black areas and the dashed line show, respectively, the model topography and the isobath of 1000 m.

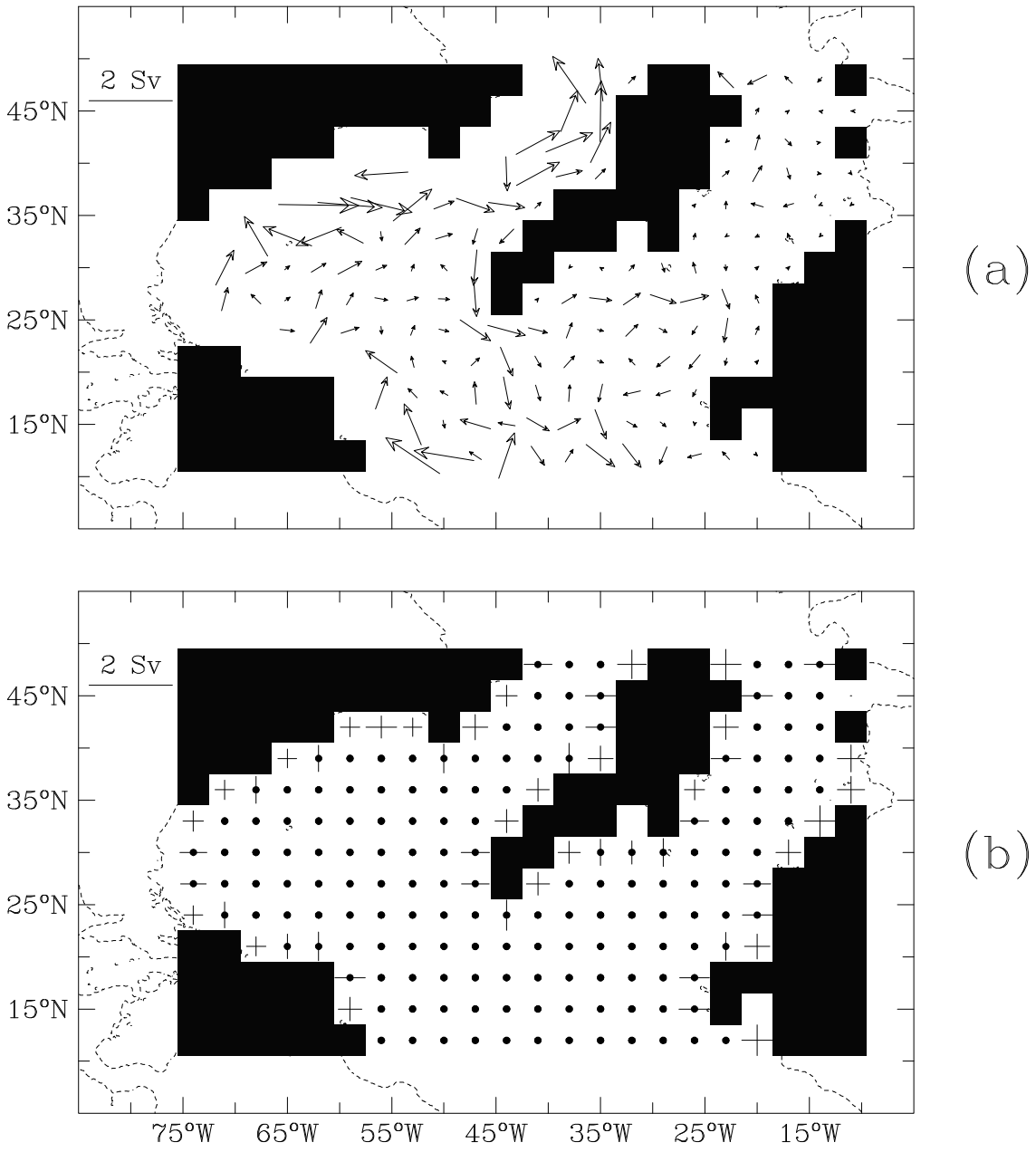

Figure 8: Same as Figure 7 but for the layer between 3000 and 4000 m.

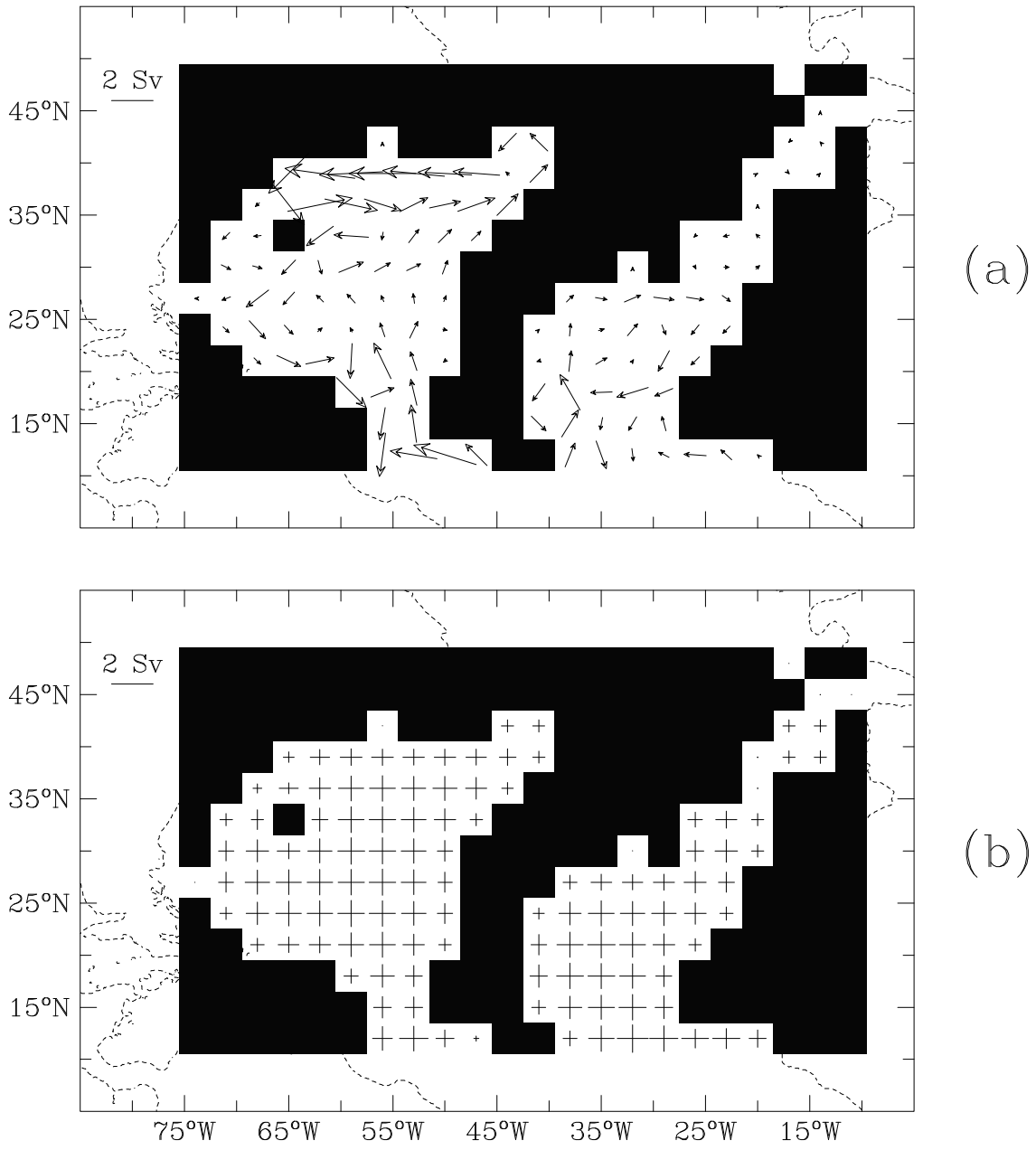

Figure 9: Same as Figure 7 but for the layer between 4000 and 5000 m. Here all vectors are shown.

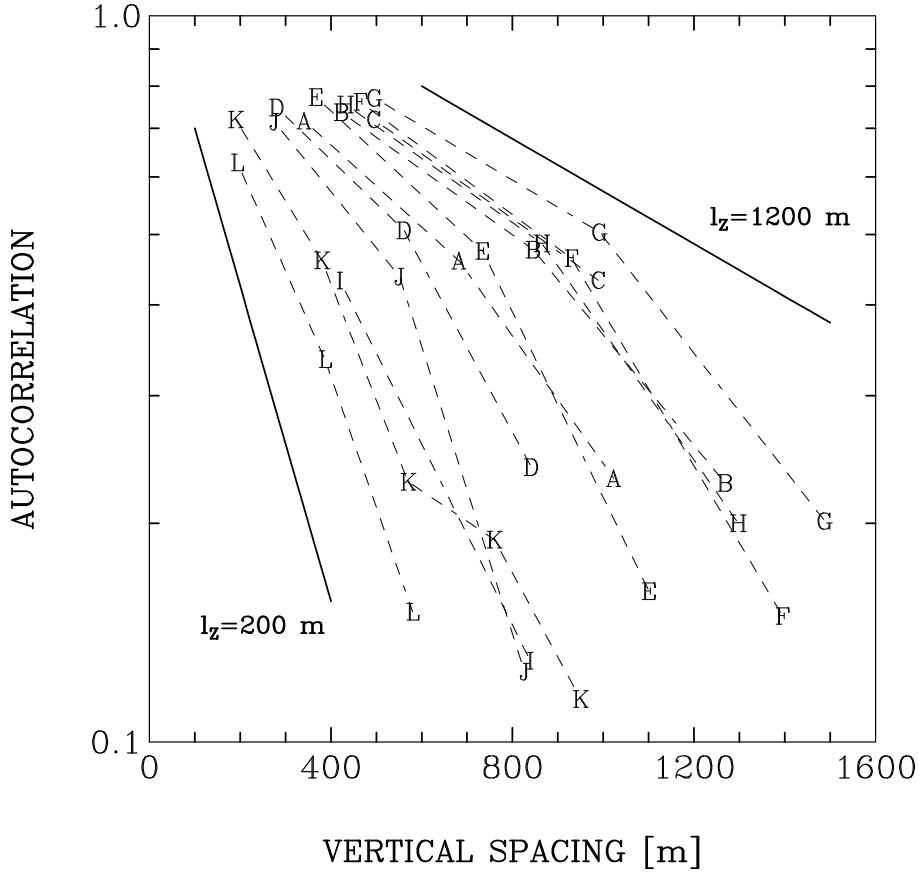

Figure 10: Leading coefficients of autocorrelation for the ^{230}Th profiles shown in Figure 2 (12 profiles). The coefficients for the same profile are connected by dashed line segments, each profile being represented by a different letter (A–L). The theoretical autocorrelation functions characterized by a vertical correlation scale $l_Z = 200$ m and $l_Z = 1200$ m are also shown (solid lines; note that the positions of both lines in the figure are arbitrary).

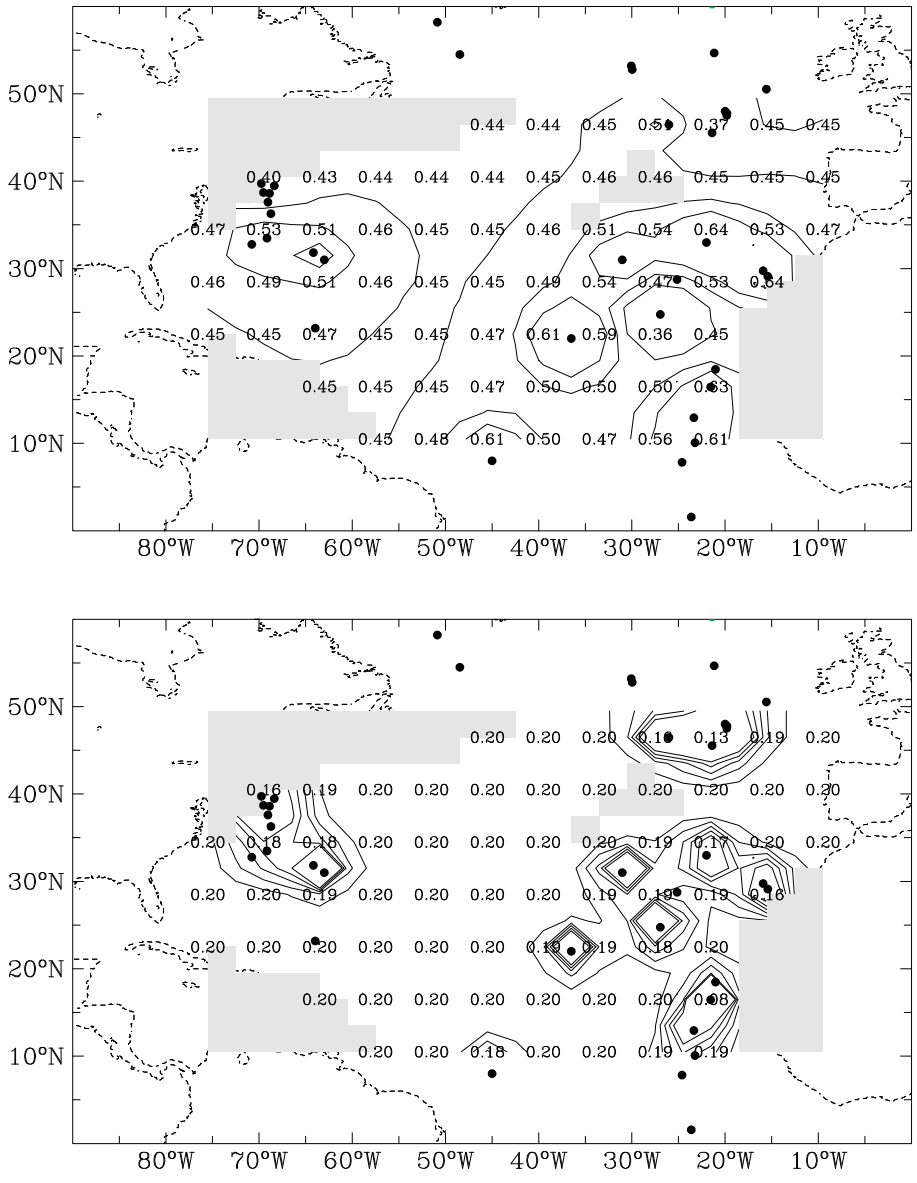

Figure 11: Distribution of (a) total ^{230}Th activity and (b) its error at $z = 3000$ m in the Atlantic between 10.5°N and 49.5°N as estimated by objective mapping for the case of small correlation scales. Only a subset of the gridded values (in units dpm m^{-3}) are shown to avoid congestion of the figure (the complete distribution has a resolution of 3° × 3° and includes values at all boundaries). No labels are reported on the isopleths, which therefore reveal only the structure of the fields. Also shown are the coastline (dashed line), the data locations (dots), and the model topography (shaded areas).

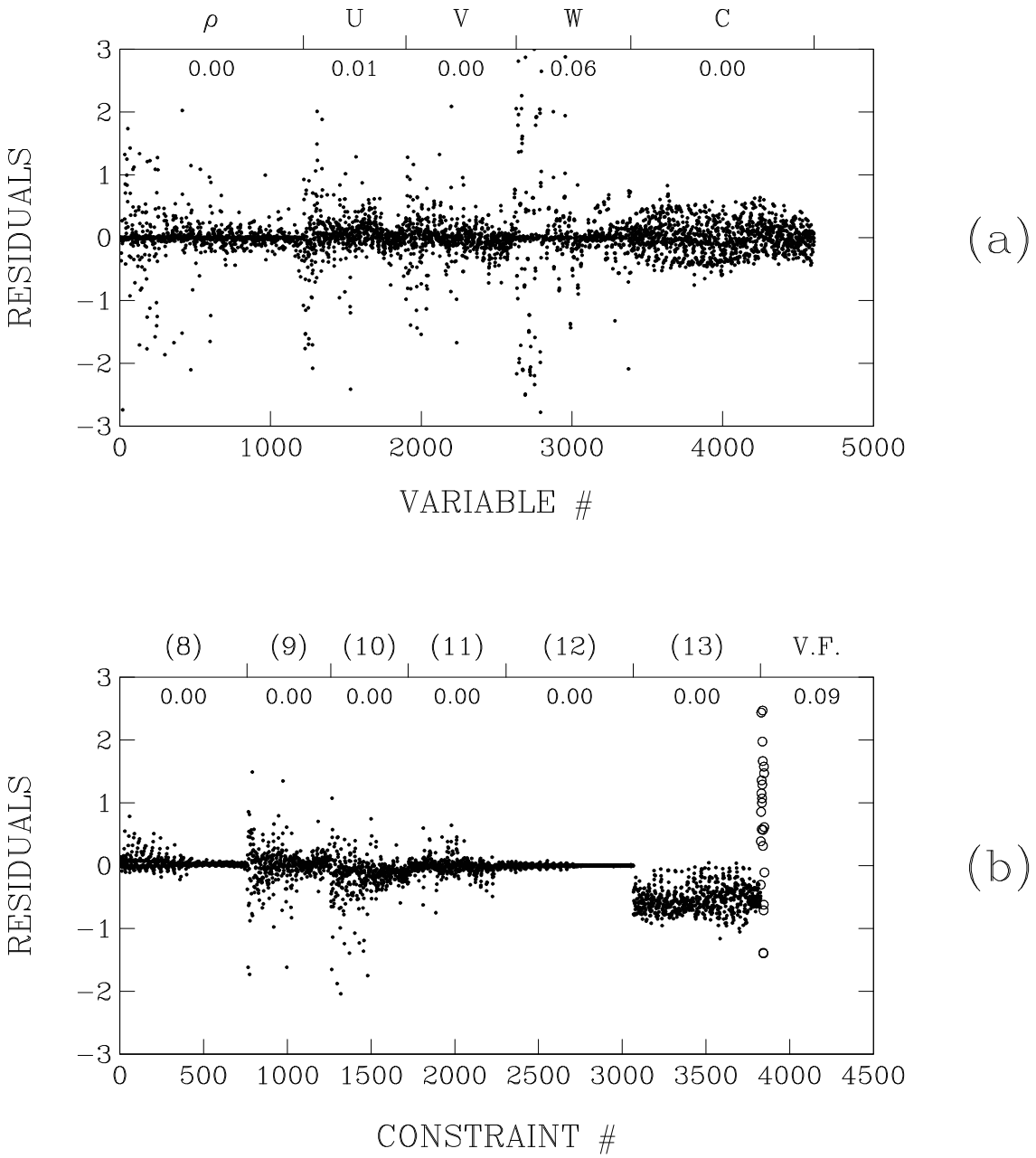

Figure 12: Diagnostics of the simultaneous inversion of density and ^{230}Th data. (a) Normalized residuals for density (ρ), the three transport components (U, V, W), and the ^{230}Th activity (C). (b) Normalized residuals for the dynamical balances (8–12) (solid circles), the radiochemical balance (13) (solid circles), and the volume transports along the western boundary (V.F.; open circles). For each panel, the values below the top horizontal axis are the fractions of normalized residuals that are ≥ 2 in absolute magnitude.

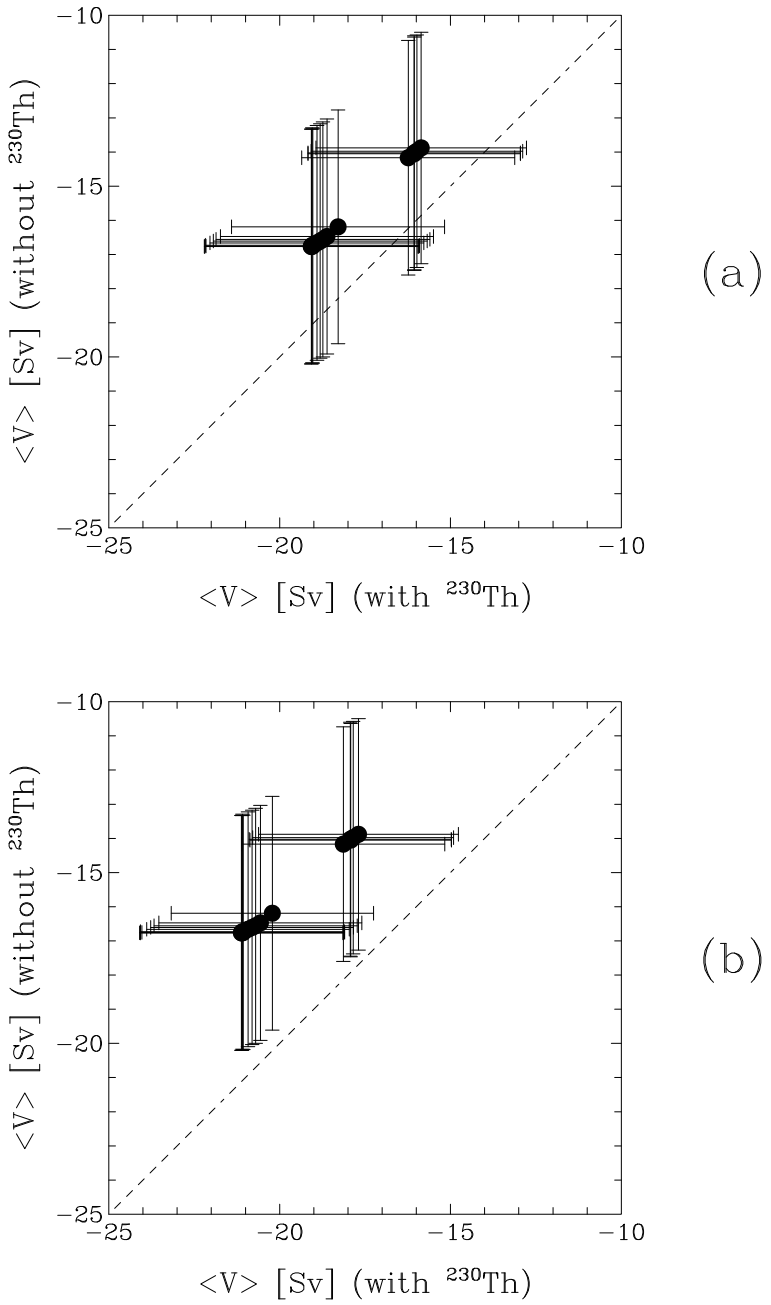

Figure 13: Comparison between the integrated meridional transports inferred without considering ^{230}Th data (vertical axis) and by considering ^{230}Th data assuming low correlation scales for their objective mapping (horizontal axis). Comparison is made for the cases where the error in the radiochemical balance (13) is 0.1 Sv dpm m^{-3} (panel a) and 0.075 Sv dpm m^{-3} (panel b). The error bars represent one standard deviation. The dashed line is the line of perfect agreement.

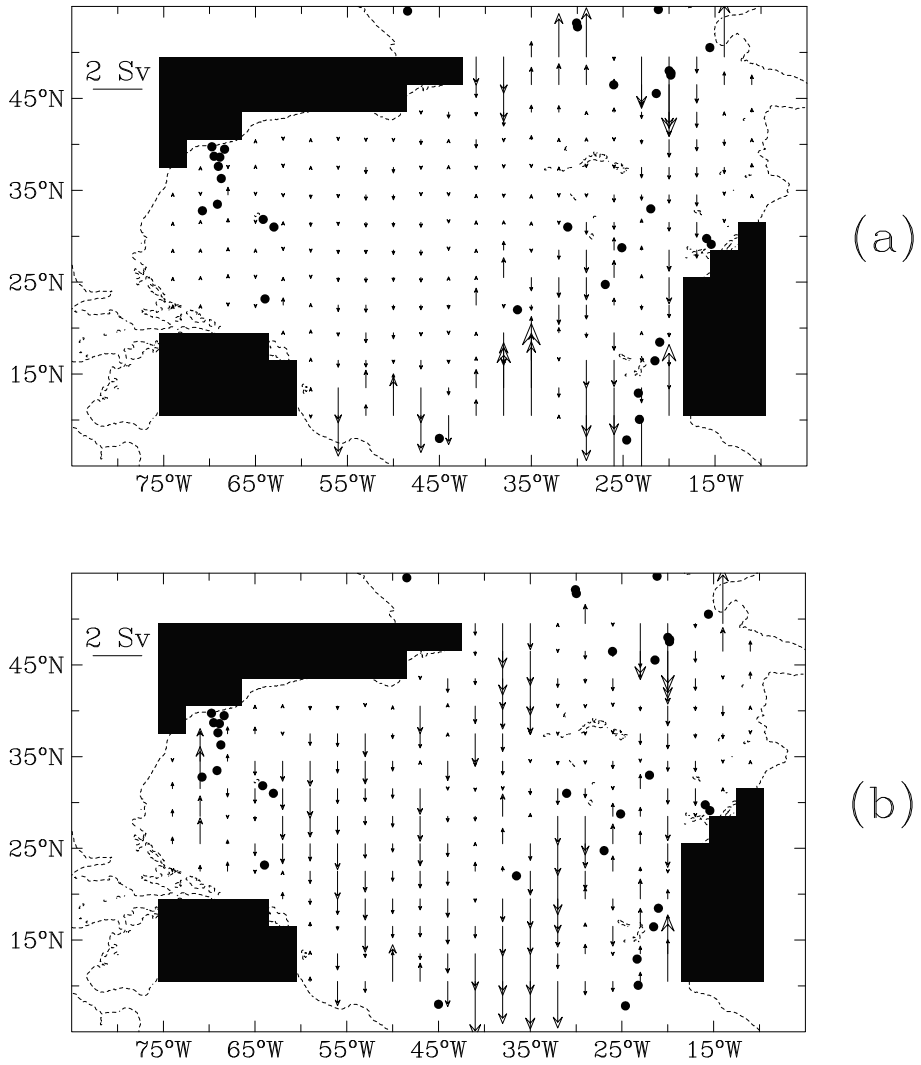

Figure 14: Distribution of the difference in the meridional component of the transport integrated over the four abyssal layers (between 1000 and 5000 m) between the simultaneous inversion of density and ^{230}Th data and the inversion of density data (reference inversion). An arrow directed southward means that the integrated transport is more to the south if ^{230}Th is considered. The transport differences are shown for the cases where small and high correlation scales are assumed in ^{230}Th mapping (respectively, panel a and panel b). For both cases, a standard deviation of 0.1 Sv dpm m^{-3} is assumed for the radiochemical balance (13). The black areas, the dashed line, and the black circles show, respectively, the model topography, the 1000 m isobath, and the stations where ^{230}Th data are available.

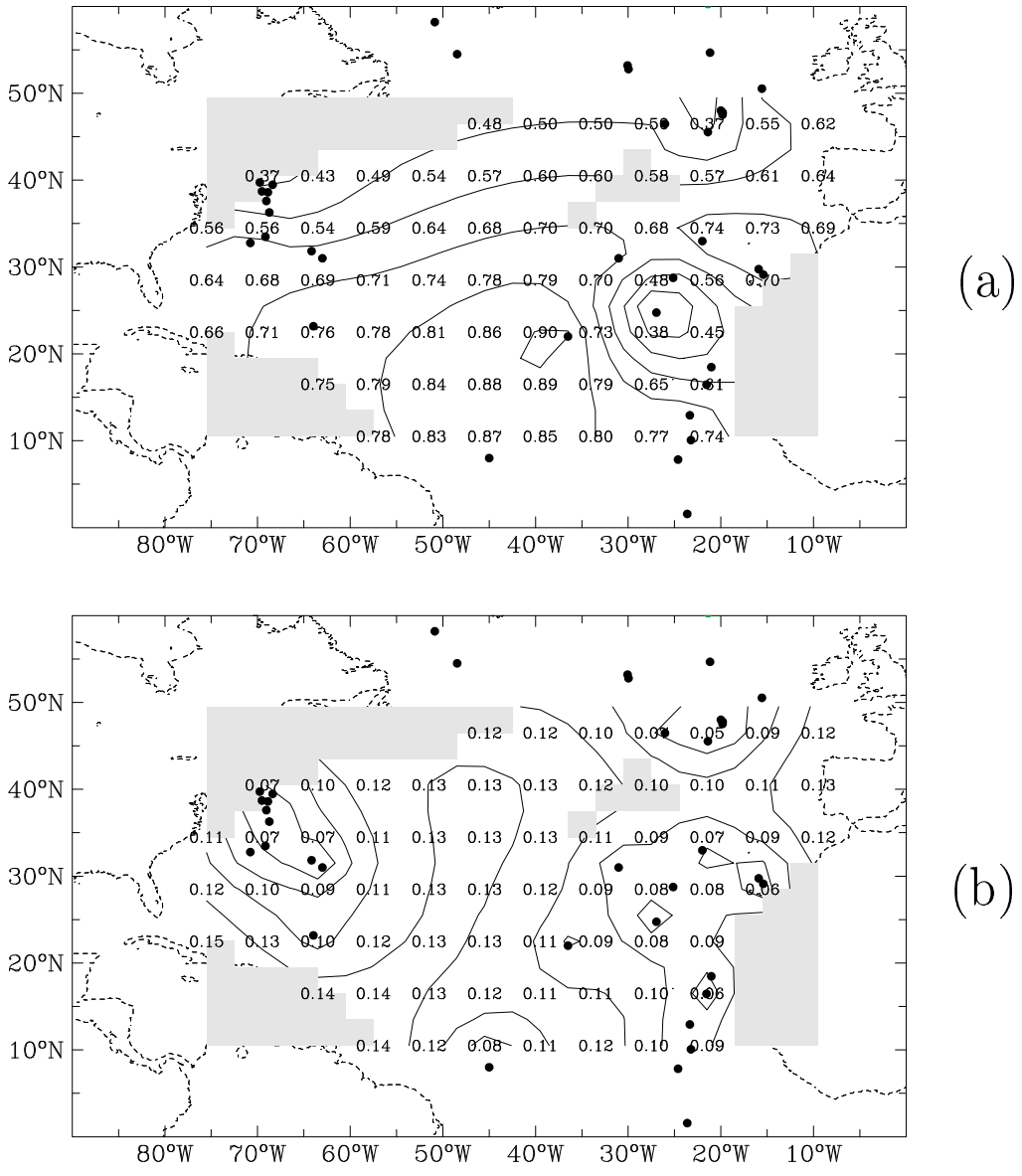

Figure 15: Distribution of (a) total ^{230}Th activity and (b) its error at z = 3000 m in the Atlantic between 10.5°N and 49.5°N as estimated by objective mapping for the case of high correlation scales. Only a subset of the gridded values (in units dpm m^{-3}) are shown to avoid congestion of the figure (the complete distribution has a resolution of 3° × 3° and includes values at all boundaries). No labels are reported on the isopleths, which therefore reveal only the structure of the fields. Also shown are the coastline (dashed line), the data locations (dots), and the model topography (shaded areas).

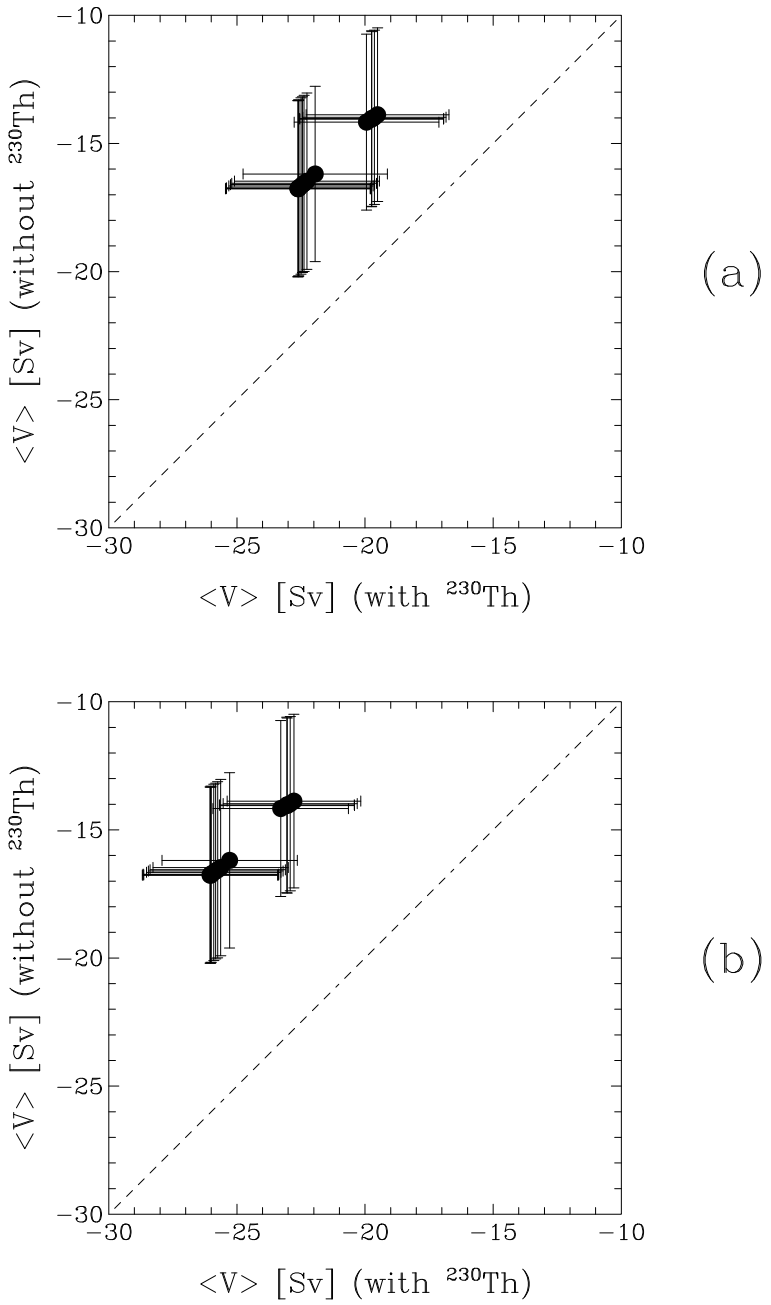

Figure 16: Comparison between the integrated meridional transports inferred without considering ^{230}Th data (vertical axis) and by considering ^{230}Th data assuming high correlation scales for their objective mapping (horizontal axis). Comparison is made for the cases where the error in the radiochemical balance (13) is 0.1 Sv dpm m^{-3} (panel a) and 0.075 Sv dpm m^{-3} (panel b). The error bars represent one standard deviation. The dashed line is the line of perfect agreement.

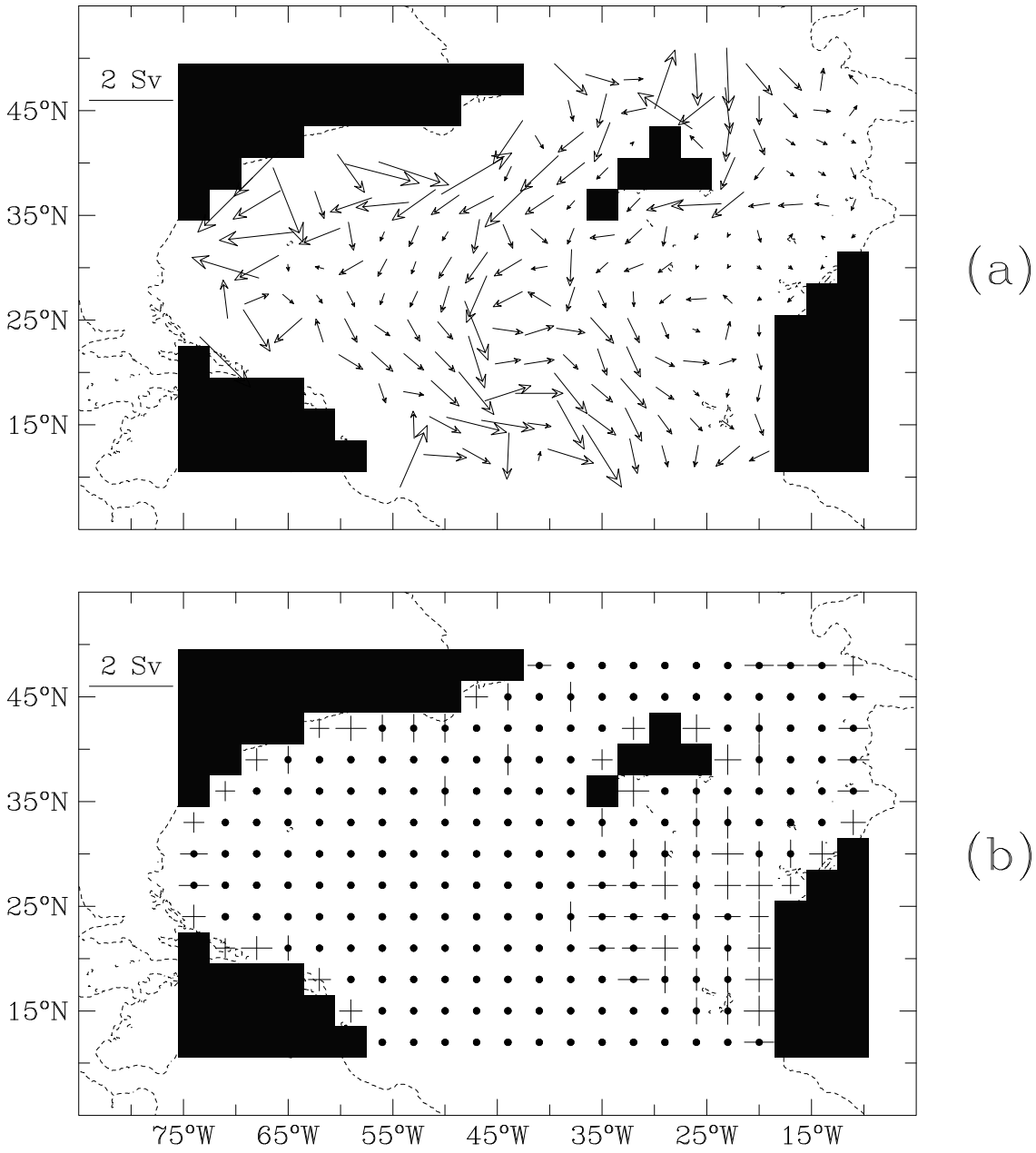

Figure 17: Distribution of (a) the horizontal transport in the layer between 2000 and 3000 m and (b) its error as estimated from the simultaneous inversion of ^{230}Th and density data. Large correlation scales are assumed for ^{230}Th mapping and the error in the radiochemical balance (13) is 0.075 Sv dpm m^{-3}. In panel (b) the horizontal (vertical) lines show the standard deviations for the zonal (meridional) components of the transport. The presence of a black dot signifies that the error in at least one component has a scale larger that the grid size (3°). The black areas and the dashed line show, respectively, the model topography and the 1000 m isobath.

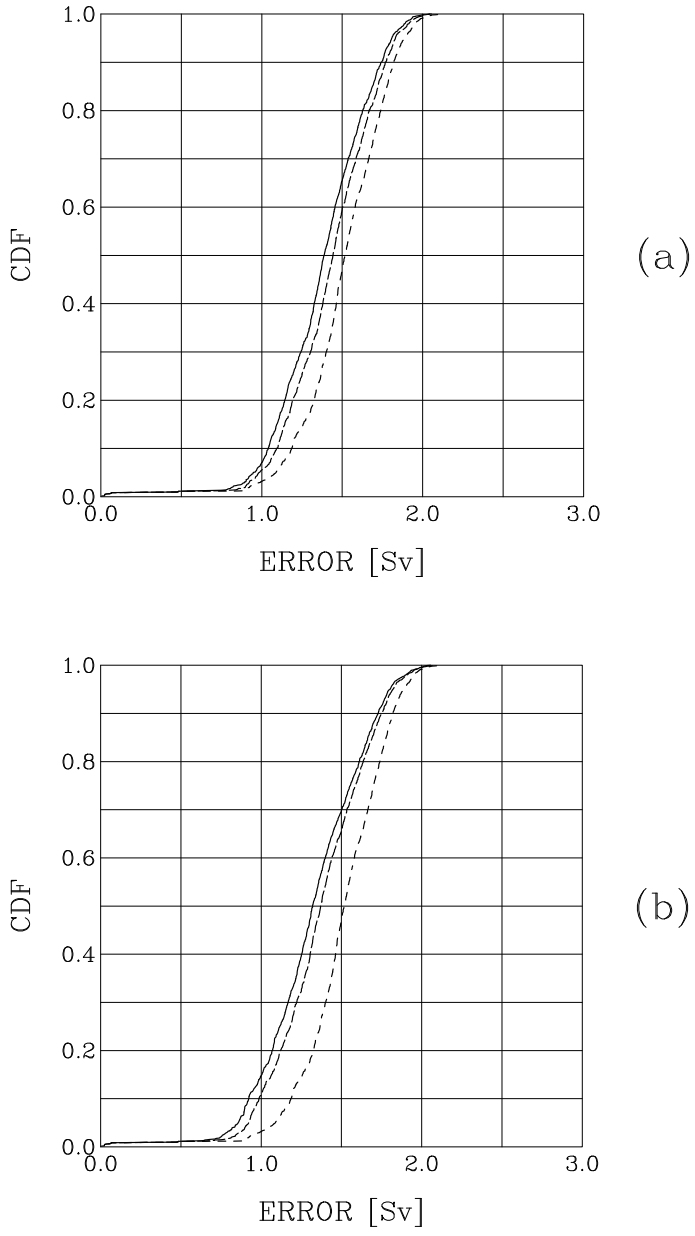

Figure 18: Cumulative distribution functions of the errors in the individual horizontal transports estimated from the inversion of density data (short dashed line) and from the simultaneous inversion of density and ^{230}Th data assuming a standard deviation of 0.1 Sv dpm m^{-3} (long dashed line) and 0.075 Sv dpm m^{-3} for the radiochemical balance (13) (solid line). (a) Case with small correlation scales for ^{230}Th mapping. (b) Case with high correlation scales for ^{230}Th mapping.

Table 1. Compilation of water column ^{230}Th data for the North Atlantic (0°–60°N)

Station[A]	*Station*[B]	*Dissolved*	*Particulate*	*Total*	
Site D	D	√			*Anderson et al.* (1983b)
Site 513	513			√	*Mangini and Key* (1983)
Site 515	515			√	-
CMME-13	CMME	√	√		*Cochran et al.* (1987)
Nares-1	NARES	√	√		-
Station 11880	BOFS	√	√		*Colley et al.* (1995)
IOC-93 Stn. 2	IOC2	√	√		*Moran et al.* (1997)
L1 (Meteor)	L1			√	*Vogler et al.* (1998)
L2 (Valdivia)	L2	√	√		-
L2 (Meteor)	L2			√	-
L3 (Poseidon)	L3	√	√		-
L3 (Meteor)	L3			√	-
ESTOC	ES			√	*Scholten et al.* (2001)[C]
La Palma	LP			√	-
IOC-6	IOC6	√	√		*Moran et al.* (2002)
Labrador Sea	LS	√	√		-
BATS	BATS			√	Buesseler & Edwards (unpub.)
KNR-07 Stn. 4	KN4	√			R. François (unpub.)
KNR-07 Stn. 5	KN5	√			-
KNR-07 Stn. 6	KN6	√			-
KNR-07 Stn. 7	KN7	√			-
KNR-07 Stn. 8	KN8	√			-
KNR-07 Stn. 9	KN9	√			-
OC-278 Stn. 2	OC2			√	-
OC-278 Stn. 3	OC3			√	-
OC-278 Stn. 4	OC4			√	-
OC-278 Stn. 5	OC5			√	-
EN-328 Stn. 4	EN4	√			-
EN-328 Stn. 7	EN7	√			-
EN-328 Stn. 9	EN9	√			-
EN-407 Stn. 3	E3	√			-
EN-407 Stn. 4	E4	√			-
EN-407 Stn. 6	E6	√			-
Stn. 331	331			√	J. Scholten (unpub.)
Stn. 355	355			√	-
Stn. 364	364			√	-
Stn. 370	370			√	-
Stn. 393	393			√	-

[A] Original name

[B] Name given in this work (Figure 1)

[C] The additional measurement at $z = 2000$ m at station L1 is included here

Table 2. Quantities used to estimate the errors of in situ densities from *HydroBase* *

z m	ρ kg m^{-3}	α 10^{-4}°C^{-1}	$\partial\rho/\partial T = -\rho\alpha$ 10^{-4}kg m^{-3}	$\partial\rho/\partial S$ kg m^{-3}
1000	1031.958	1.559	–1609	0.781
2000	1036.903	1.469	–1523	0.781
3000	1041.649	1.494	–1556	0.778
4000	1046.017	1.707	–1786	0.771
5000	1050.293	1.907	–2003	0.764

* Based on (i) the mean in situ temperature (T) and salinity (S) at each depth according to *HydroBase* and (ii) the parameters of the equation of state of *Gill* (1982) (Table A3.1).